STScI | SPACE TELESCOPE SCIENCE INSTITUTE

JWST TECHNICAL REPORT

Title: The Ghosts of NIRISS: Imaging	Doc #: JWST-STScI-004877, SM-12 Date: 20 December 2018 Rev: -
Authors: André R. Martel Phone: 410-338-4888	Release Date: 22 January 2019

1 Abstract

We present and characterize optical ghosts observed in direct images with the Near-Infrared Imager and Slitless Spectrograph (NIRISS) during the ground cryo campaigns at the Goddard Space Flight Center (GSFC) and the Johnson Space Center (JSC). The ghosts exhibit a wide range of morphologies, from out-of-focus PSFs to extended and clumpy structures, that vary over the field of view (FOV). They are distributed about a specific axis in each filter, as predicted by the optical models. Knowledge of the coordinates of the intersection of this axis on the detector, the Ghost Axis Point (GAP), can help map the location of the ghosts. The GAP of the double-stack filters in the pupil wheel (PW) is near the field center, albeit slightly offset, while the GAP of the single-stack filters in both wheels is located closer to the edges of the field. The filters in the filter wheel (FW) may also possess a second GAP near the field center, possibly due to reflections from the the pupil alignment reference (PAR). Because the GAP is not at the exact field center, there are areas where a bright astronomical source will not produce a ghost on the detector. In the third cryo-vacuum campaign (CV3) at GSFC, the ratio of the integrated counts between the ghosts and their point spread functions (PSFs) is about 0.2 – 1.5%. But the extended sources observed in the cryo campaign of the Optical Telescope Element/Integrated Science Module (OTIS) at JSC produced ghosts with significantly higher ratios, 0.8 – 25%. The source of this discrepancy is unknown. We find no convincing radial dependence of this ratio with distance from the GAP. We briefly discuss strategies to mitigate the impact of ghosts on astronomical sources. In the commissioning campaign and in the subsequent regular operations, a thorough characterization of the ghosts will be possible as a variety of astronomical sources are imaged over the entire FOV.

2 Introduction

Complex optical systems often suffer from single or multiple internal reflections which will form a duplicate image of the source at the focal plane. These “ghosts” often appear blurry, e.g., out-of-focus, and their morphologies and brightness may vary over the field of view (FOV) depending on the optical element, e.g., a filter or grism, in the light path. An unfortunate and painful consequence of ghosts is the contamination of an astronomical scene – a ghost can be

Operated by the Association of Universities for Research in Astronomy, Inc., for the National Aeronautics and Space Administration under Contract NAS5-03127

confused with a true astronomical source or overlap with a source in a crowded field. Accurate photometric measurements become difficult, perhaps even questionable, since a fraction of the light of a source is redirected in a ghost elsewhere in the field and is likely not recoverable.

In this report, we characterize the ghosts associated with the majority of the broad- and narrow-band filters of NIRISS using data collected in the cryo campaign of the Optical Telescope Element/Integrated Science Module (OTIS) at the Johnson Space Center (JSC) in Jul – Oct 2017 and in the third cryo campaign (CV3) of the Integrated Science Instrument Module (ISIM) at the Goddard Space Flight Center (GSFC) in Nov 2015 – Feb 2016. For these two test campaigns, NIRISS was in its final flight configuration. We also supplement these datasets with those of the first and second cryo campaigns at GSFC, CV1RR (Sep – Oct 2013) and CV2 (Jul – Sep 2014). We summarize the morphology, location, and when possible, the relative counts of the ghost with respect to its source.

This characterization of the ghosts in the multiple optical elements of NIRISS is preliminary because of the limitations of the ground test environment and schedule (time constraints, source pointings and fluxes, etc…). But it offers a preview of the ghosts that we expect to detect and monitor in the much richer on-orbit observations and it provides some information to the observers on the potential impact of the ghost contamination. We note that we do not consider stray light or glints that can be produced when a bright source is positioned immediately outside the FOV – no such features have been observed with NIRISS in the ground activities.

For reference, a diagram of the NIRISS dual wheel (DW), which consists of the pupil wheel (PW) and the filter wheel (FW), is shown in Fig. 2-1. The single-stack filters (F480M, F380M, F430M, F356W, F444W, and F277W) and the GR150C/R grisms in the FW, as well as the single-stack F158M filter in the PW, are tilted by about 2° to minimize the areas on the detector where ghosts can be imaged (Aldridge et al. 2011). On the other hand, the double-stack filters (F090W, F115W, F140M, F150W, and F200W) in the PW are not tilted. For the Wide Field Slitless Spectroscopy (WFSS) mode, the two grisms GR150C and GR150R can be crossed with the six blocking filters F090W, F115W, F158M, F140M, F150W, and F200W. For the Single Object Slitless Spectroscopy (SOSS) mode, the GR700XD grism is combined with the CLEAR aperture (although for calibration, it may be paired with F277W to isolate the red end of the 1st order of the spectrum). The Aperture Masking Interferometry (AMI) mode allows crossing the non-redundant mask (NRM) with F480M, F380M, F430M, or F277W. For simple imaging, a PW filter is combined with CLEAR or a FW filter with CLEARP, which holds the pupil alignment reference (PAR).

Most of our interpretation of the ghosts is based on FRED (Photon Engineering) models developed by Hill et al. (2013a) and Rohrbach & Irvin (2014). For imaging, the ghosts are primarily due to reflections from the detector to the filter in the DW and back to the detector. For some red filters in the FW that are crossed with CLEARP in the PW, some ghosts can result from scattering on the back of the PAR. In a future report, we will present the ghosts detected in the grism exposures: GR150C and GR150R for the WFSS mode and GR700XD for the SOSS mode.

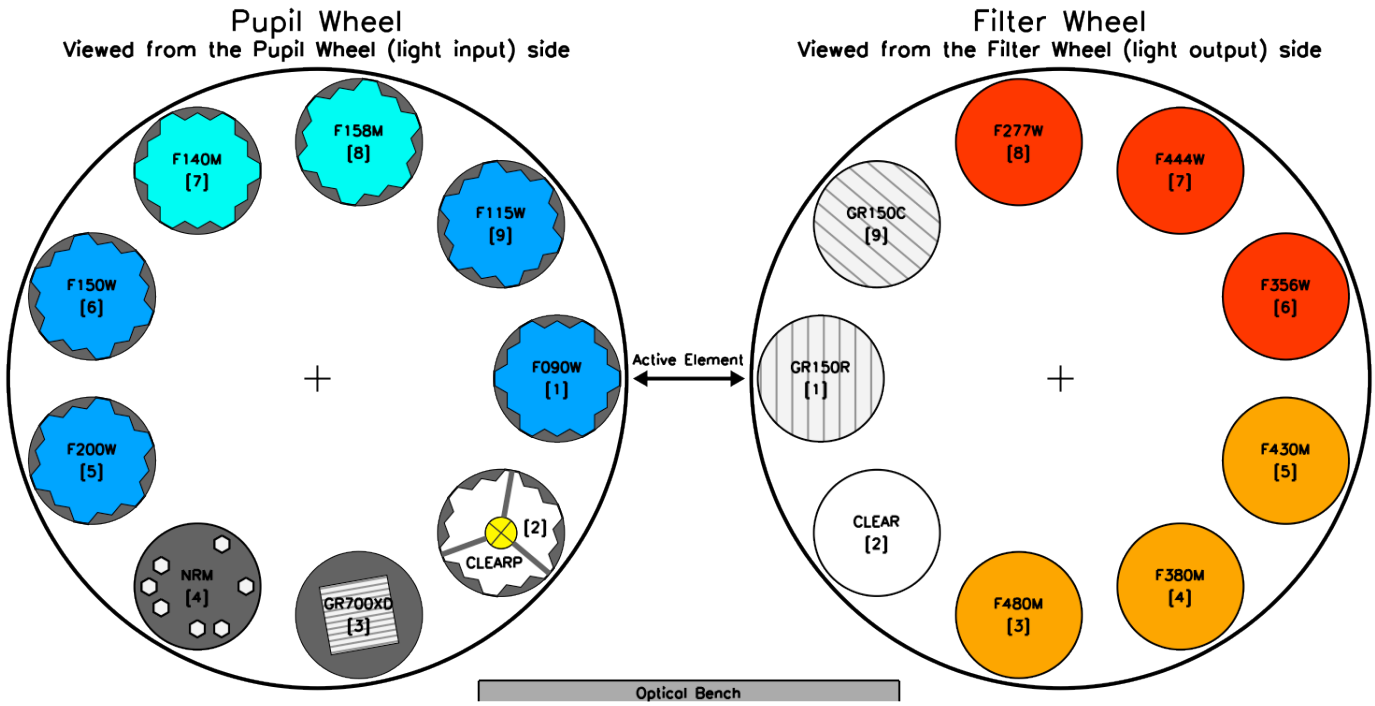

Figure 2-1. Schematic of the NIRISS Dual Wheel (DW). In the light path of NIRISS, a photon traverses the PW before the FW. The double-stack filters are F090W, F115W, F140M, F150W, and F200W in the Pupil Wheel (PW).

3 The Ghost Axis Point (GAP)

For a given filter, the optical models predict a specific location in the FOV about which the ghost is "reflected" from the source. It is called the Ghost Axis Point (GAP) and is simply located at the midpoint of the line joining the source and its ghost. Knowledge of the coordinates of the GAP can provide powerful information for mapping the ghosts anywhere in the field and can prove useful for decontaminating a crowded field, for example. This behavior also means that there are regions in the FOV far enough from the GAP where a source will produce a ghost outside the FOV and no contamination of the field will ensue. In practice, the location of the GAP can be found by simply observing a bright source and measuring the midpoint to its ghost. In general, the location of the ghost about the position of the GAP:

$$X_{Ghost} = 2\,X_{GAP} - X_{Source}$$
$$Y_{Ghost} = 2\,Y_{GAP} - Y_{Source}$$

where (X_{source}, Y_{source}) is the coordinate of the bright source. This transformation corresponds to a $\approx 180°$ rotation or a left-to-right flip followed by and top-to-bottom flip (or vice-versa) about the GAP as the pivot point. In this report, we provide the coordinates of this critical field point for the different filters.

4 Calibration

The OTIS and CV3 exposures were processed in a similar manner with standard pipeline steps. All the arrays are full-frame (2048×2048; $t_f = 10.737$ sec) to ensure that the ghosts are captured within the NIRISS FOV. The 0th -frame (or "bias" or "pedestal) of each integration was subtracted from all the subsequent groups of the integration to remove the kTC noise and other correlated noise. The level of the imaging area of each group was then adjusted with the mean

value of the horizontal reference pixels. The counts in each pixel were then corrected for the non-linear response of the detector with linearity coefficients calculated from the deep, well-sampled OSIM flat fields collected in OTP 7.17 Detector Linearity in CV3.

In the CV3 campaign, the Optical Telescope Element (OTE) Simulator (OSIM; Davila et al. 2008; Sullivan et al. 2010) produced accurate PSFs while in the OTIS campaign, the Aft Optical Subsystem (AOS) Source Plate Assembly (ASPA) delivered extended sources. These broad-band or monochromatic sources were generated either with a constant or pulsed illumination. In CV3, the slopes of the low-flux PSFs or 1st-order spectra were calculated from the groups with raw peak counts below the digital saturation of 65525 ADUs/pixel. For the high-flux sources, which usually saturated strongly, all the groups were included in the slope calculations to maximize the S/N ratio of the weak ghosts. None of the extended OTIS sources considered in this report reached saturation. For the pulsed sources, no slopes were calculated and the last unsaturated group of the integration was used. The direct images collected in CV3 were flat-fielded with similarly calibrated and normalized images of flats collected in OTP 7.4, 7.4 Rev A, and 7.4 Rev B OSIM Flat Fields. The OTIS images were not flat-fielded because of the obscuration of a large section of the FOV by the ASPA module. The background exposures, treated in the same manner, albeit with no constraints on their slopes, were finally subtracted.

The CV1RR and CV2 exposures, collected with a different detector and suffering from a heavy population of bad pixels, were calibrated with the same basic steps but with no linearity and flat field correction.

5 Characterization of the Ghosts

The images were inspected for evidence of ghosts in the FOV and when positively identified, these properties were characterized:

1. Location: The coordinates of both the source and its ghost on the detector were measured with flux-weighted centroids. The half-way field point marks the location of the GAP. In this report, the figures and coordinates are oriented in the coordinate system produced by the JWST calibration pipeline (+V1 into the page, +V2 to the left, and +V3 to the top and the (1, 1) origin in the bottom-left corner for a 2048×2048 array).
2. Morphology: The overall morphology of the ghost is qualitatively described (circular vs elongated, asymmetry, diameter, etc…).
3. Ratio of counts: When possible, the relative counts of the ghost with respect to its primary source was calculated. For the extended sources in the OTIS campaign, small boxes were defined about the centroid of the ghost and its source and the total counts were summed and ratioed in each box after subtracting a nearby background box of the same dimensions. No significant differences in the counts and ratios were found by varying the size of the boxes. Bad pixels (primarily resistor-capacitor (RC), random telegraph noise (RTN), and hot pixels) were excluded with a bad-pixel map generated from CV3 darks. For the PSFs of CV3, we found that scaling the low-flux PSF to the high-flux PSF using isophotes was generally unreliable because the low-flux PSF is entirely contained within the saturated core of the bright PSF – there is no common region outside the saturated core for an accurate extraction of the wing profiles. Instead, we simply used the scaling factor from the Test Planning Tool (TPT) (see Appendix 2).

6 OTIS Campaign

All the exposures collected in the OTIS campaign were carefully examined for the presence of ghosts. Positive identifications were found for the four broad-band filters of the WFSS mode (F090W, F115W, F150W, and F200W) and are summarized in Table A1-1 of Appendix 1. The

coordinates of the sources, ghosts, and GAP, as well as the ghost/source count ratios are tabulated in Tables A1-1 to A1-17. Some of the fields are displayed in Figs A1-1 to A1-8. Fig. A1-4 also shows an example of the boxes defined around the source and its ghost for calculating the ratio of their counts. In a sense, the OTIS exposures are representative of an astronomical scene: many extended sources are imaged simultaneously over a large fraction of the field. In contrast, the sources in the CV campaigns are PSFs imaged at single field locations.

The sources and their ghosts are extended and clumpy and show complicated morphologies that don't match, taking into account the rotation about the GAP (see Fig. A1-7). The flux-weighted centroid of a source is therefore calculated from different clumps than those in its ghost, resulting in a relatively large uncertainty of 2 to 3 pixels in the coordinates of the GAP. For a given filter, we assume that the coordinates of the GAP have no dependence on the location of the source. In the following, we present the results of a high-level analysis of the distribution and importance of the ghosts and we report the coordinates of the GAP for the four filters.

6.1 F090W

In Table 6-1, the coordinates of the GAP for F090W are calculated as the mean of all the OTIS measurements in this filter. The coordinates are also corrected for the geometric distortion to ease the comparison with the output products of the JWST calibration pipeline. This correction includes the conversion from real to ideal pixels (Martel & Fullerton 2016) and to the telescope coordinate system (Cox et al. 2008) and is only approximate until the on-orbit updates are made. We choose the corrected bottom-left corner as the reference pixel.

Table 6-1. Coordinates of the GAP for F090W (OTIS)

GAP (X, Y)	GAP_c (X, Y)
$(1167.3 \pm 0.1, 938.6 \pm 1.4)$	$(1167.5 \pm 0.1, 933.5 \pm 1.4)$

1. The coordinates of GAP_c are corrected for the geometric distortion.

In Fig. 6-1, we show the distribution of the ASPA sources (red stars) and their ghosts (blue circles) over the NIRISS FOV. The size of the blue circles correlates with the ghost/source count ratio. The black X marks the location of the GAP. A bright source will not produce a ghost in the FOV if it is located in the green region. Or conversely, if the source falls inside the rectangle defined by $X \geq 287$ and $Y \leq 1877$ in the distorted 2048×2048 frame, then a ghost will be observed in that region.

The ratio of the counts between the ghosts and the sources are plotted as a function of the distance of the source from the GAP in Fig. 6-2. The two sources and their ghosts are observed at essentially the same location in the FOV. But surprisingly, the count ratio is very large for both, 24.6 ± 3.0 %. Unfortunately, there are no other field points at larger radii that would help us determine if this ratio decreases further away from the GAP.

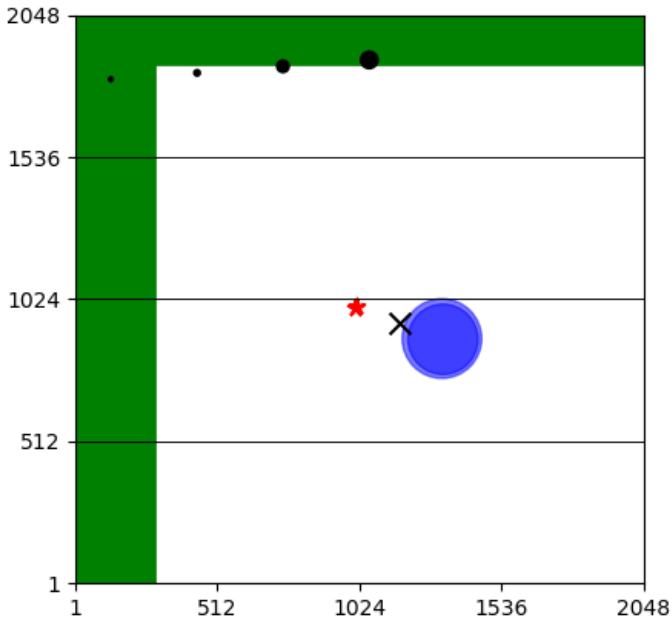

Figure 6-1. The location of the ASPA sources (red stars) and their ghosts (blue circles) are plotted for F090W (OTIS). The size of the blue circles correlates with the ghost/source count ratio. The X marks the mean location of the GAP. Inside the green area, a source will not produce a ghost in the FOV. The black circles represent the coronagraphic occulters.

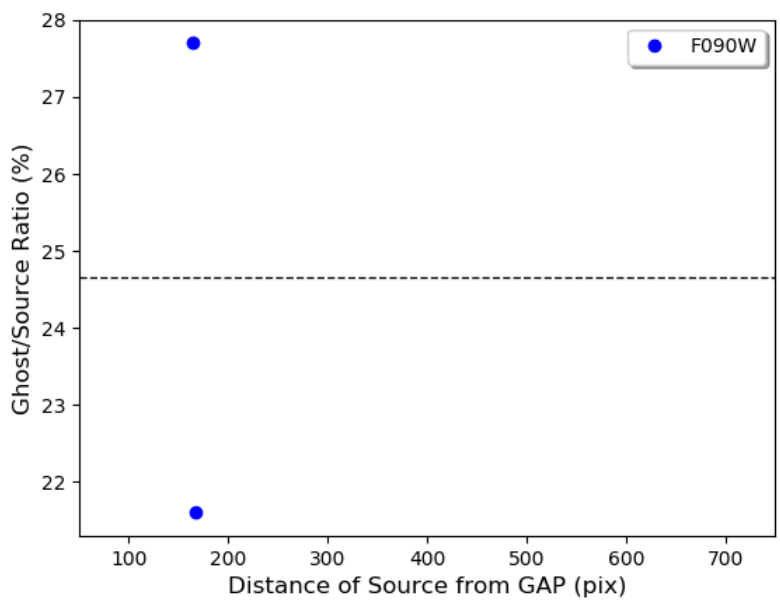

Figure 6-2. Ratio of the counts between the ghosts and sources as a function of the distance of the sources from the GAP for F090W (OTIS). The dashed line represents the mean value.

6.2 F115W

The results for the OTIS measurements of F115W filter are summarized in Table 6-2 and Figs. 6-3 and 6-4. A ghost will be observed if the source falls in the region defined by $X \geq 249$ and $Y \leq 1855$. The two sources and their ghosts are observed at essentially the same location in the FOV. The count ratio is relatively large, 3.2 ± 0.8 %.

Table 6-2. Coordinates of the GAP for F115W (OTIS)

GAP (*X*, *Y*)	GAP_c (*X*, *Y*)
(1148.6 ± 0.4, 927.3 ± 0.1)	(1148.8 ± 0.4, 922.3 ± 0.1)

1. The coordinates of GAP_c are corrected for the geometric distortion.

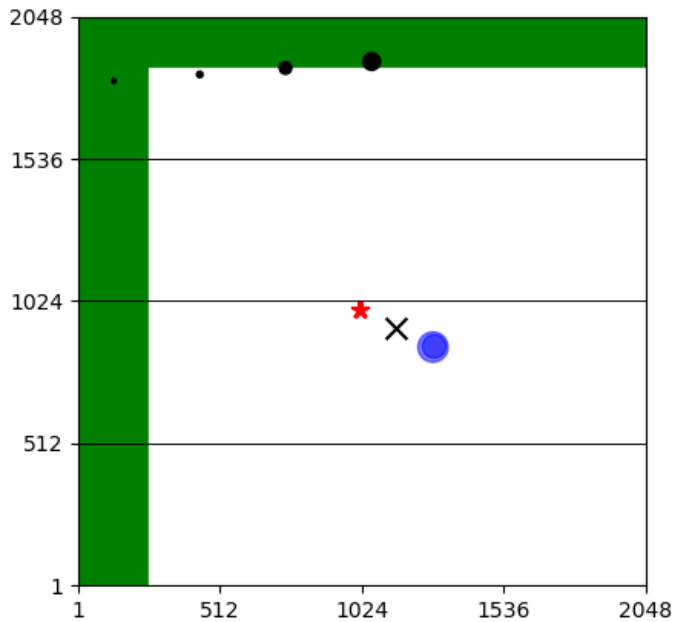

Figure 6-3. Same as Fig. 6-1 but for F115W (OTIS).

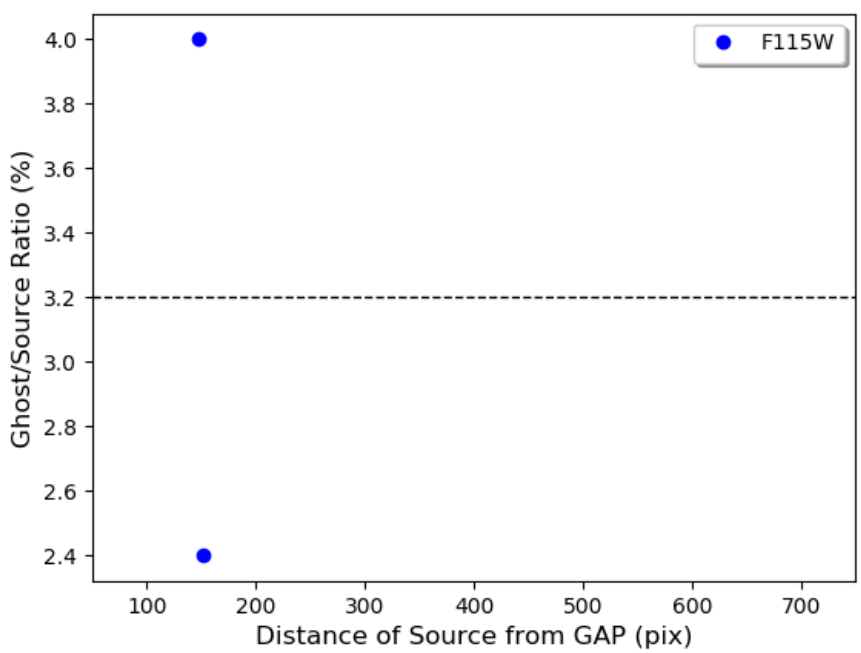

Figure 6-4. Same as Fig. 6-2 but for F115W (OTIS).

6.3 F150W

The results for the OTIS measurements of F150W filter are summarized in Table 6-3 and Figs. 6-5 and 6-6. A ghost will be observed if the source falls in the region defined by $X \geq 275$ and $Y \leq 1875$. The ratio shows no clear trend with distance, at least over the interval of ~150 to 700 pixels. The mean ratio is relatively small, 0.80 ± 0.24 %.

Table 6-3. Coordinates of the GAP for F150W (OTIS)

GAP (*X*, *Y*)	GAP_c (*X*, *Y*)
$(1161.8 \pm 2.5, 937.3 \pm 2.2)$	$(1162.0 \pm 2.5, 932.3 \pm 2.2)$

1. The coordinates of GAP_c are corrected for the geometric distortion.

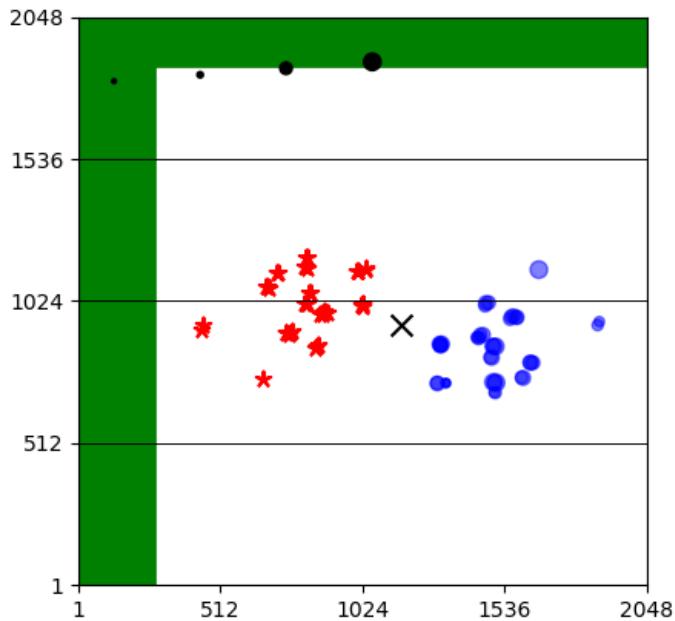

Figure 6-5. Same as Fig. 6-1 but for F150W (OTIS).

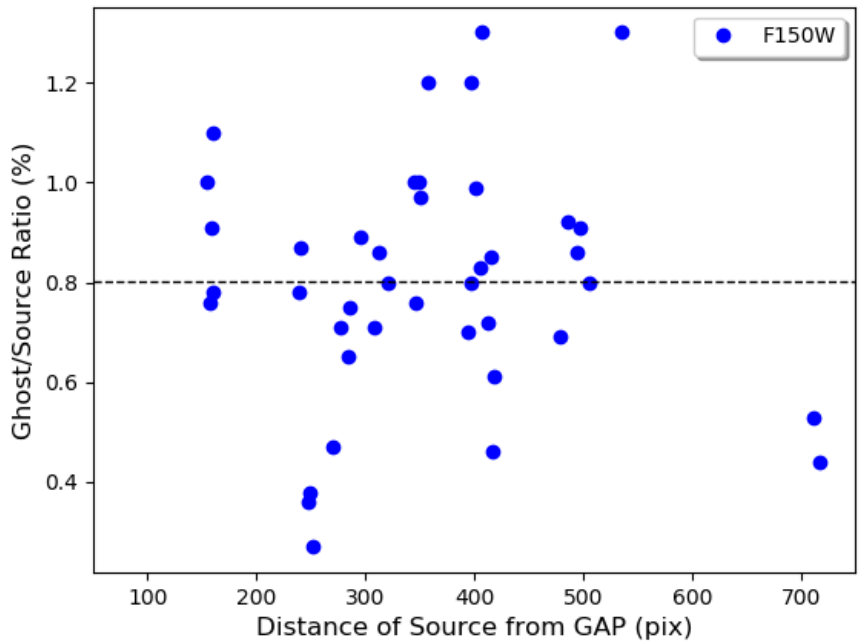

Figure 6-6. Same as Fig. 6-2 but for F150W (OTIS).

6.4 F200W

The results for the OTIS measurements of F200W filter are summarized in Table 6-4 and Figs. 6-7 and 6-8. A ghost will be observed if the source falls in the region defined by $X \geq 265$ and $Y \leq 1890$. The mean count ratio is 1.3 ± 0.6 %.

Table 6-4. Coordinates of the GAP for F200W (OTIS)

GAP (*X*, *Y*)	GAP_c (*X*, *Y*)
(1156.4 ± 2.5, 944.9 ± 3.0)	(1156.6 ± 2.5, 939.9 ± 3.0)

1. The coordinates of GAP_c are corrected for the geometric distortion.

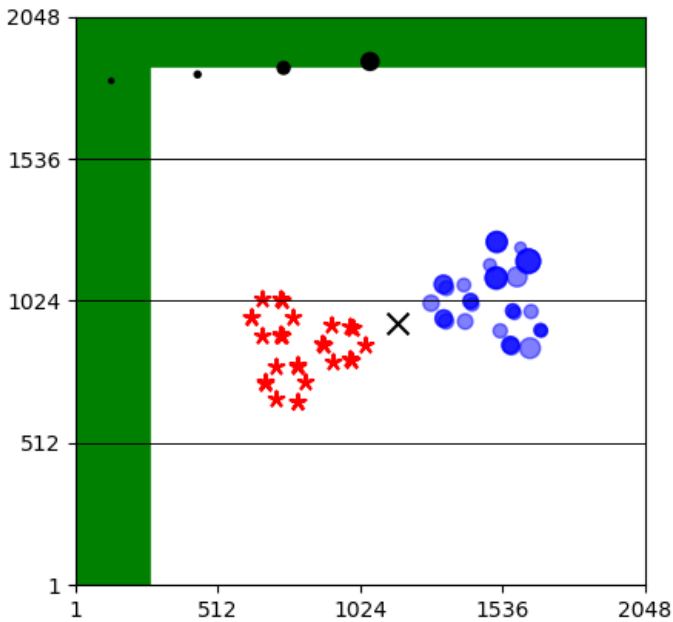

Figure 6-7. Same as Fig. 6-1 but for F200W (OTIS).

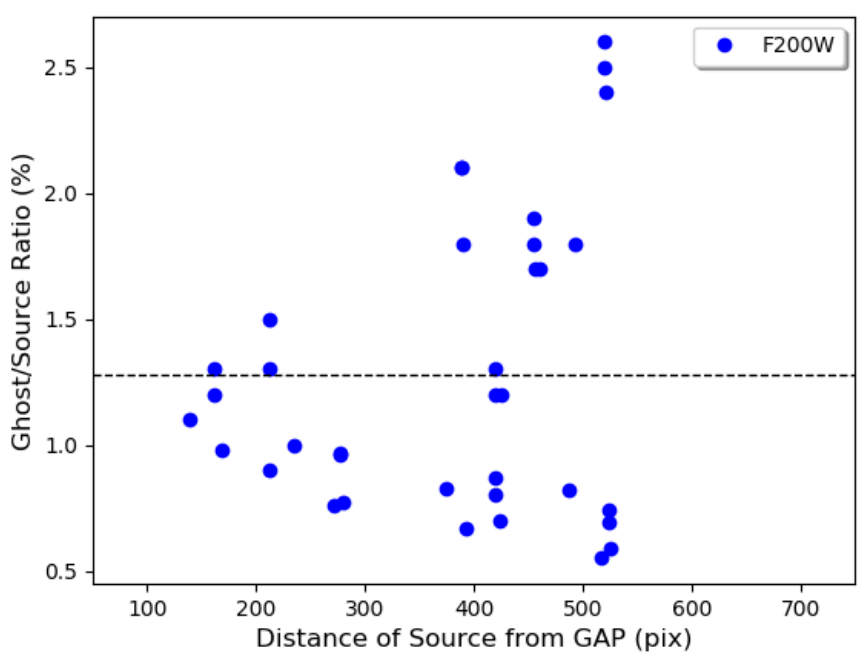

Figure 6-8. Same as Fig. 6-2 but for F200W (OTIS).

7 CV3 Campaign

As for the OTIS campaign, all the exposures collected in the CV3 campaign were carefully examined for the presence of ghosts. The positive identifications are summarized in Table A2-1 of Appendix 2. The coordinates of the OSIM PSFs, ghosts, and GAP, as well as the ghost/source count ratios are tabulated in Tables A2-2 to A2-6. The sources and ghosts are shown in Figs. A2-1 to A2-10.

We note that high-flux PSFs were imaged in F158M and in F356W near the field center. No ghosts were detected for F158M in OTP 7.6.3 (JOBIDs = 35850 and 35857) because its GAP is near the bottom of the FOV (see Section 9; CV1RR) and the pointing of the OSIM source in these exposures would have placed the ghosts outside the FOV. Also, the scaling factor of the OSIM source between the low- and high-flux sources was only about 11, which may account for the non-detection of the F158M ghosts. The F158M filter is a single stack filter and its ghosts are not expected to behave like those of the double stack filters in the PW. Similarly, no ghost is seen in F356W (JOBIDs = 41958 and 41962) in OTP 6.5 Rev B. Although, we do not possess any other exposures in this filter to confirm the coordinates of its GAP, we suspect that it is also located near one of the edges of the FOV.

7.1 F090W

In Table 7-1, the coordinates of the GAP for F090W are calculated as the mean of all the CV3 measurements in this filter. The coordinates are also corrected for the geometric distortion to ease the comparison with the output products of the JWST calibration pipeline.

Table 7-1. Coordinates of the GAP for F090W (CV3)

GAP (X, Y)	GAP_c (X, Y)
(1169.2, 936.7)	(1169.4, 931.6)

1. The coordinates of GAP_c are corrected for the geometric distortion.

As for the OTIS campaign, in Fig. 7-1, we show the distribution of the OTIS sources (red stars) and their ghosts (blue circles) over the NIRISS FOV. The size of the blue circles correlates with the ghost/source count ratio. The black X marks the location of the GAP. A bright source will not produce a ghost in the FOV if it is located in the green region. Or conversely, if the source falls inside the rectangle defined by $X \geq 290$ and $Y \leq 1873$ in the distorted 2048×2048 frame, then a ghost will be observed in that region.

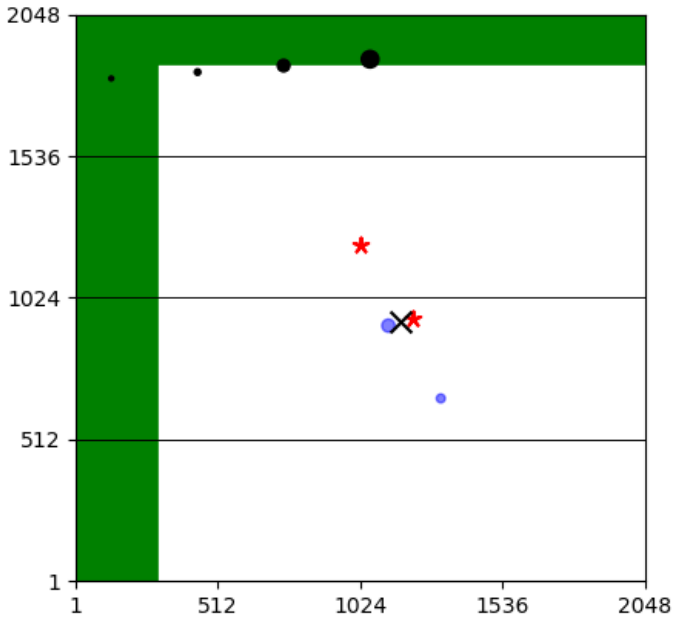

Figure 7-1. The location of the OSIM sources (PSFs; red stars) and their ghosts (blue circles) are plotted for F090W (CV3). The size of the blue circles correlates with the ghost/source count ratio. The X marks the mean location of the GAP. Inside the green area, a source will not produce a ghost in the FOV. The black circles represent the coronagraphic occulters.

7.2 F115W

The results for the CV3 measurements in the F115W filter are summarized in Table 7-2 and in Fig. 7-2. A ghost will be observed if the source falls in the region defined by $X \geq 262$ and $Y \leq 1856$. The count ratio is significantly smaller than in the OTIS data.

Table 7-2. Coordinates of the GAP for F115W (CV3)

GAP (*X*, *Y*)	GAP$_c$ (*X*, *Y*)
(1155.0, 928.1)	(1155.2, 923.1)

1. The coordinates of GAP$_c$ are corrected for the geometric distortion.

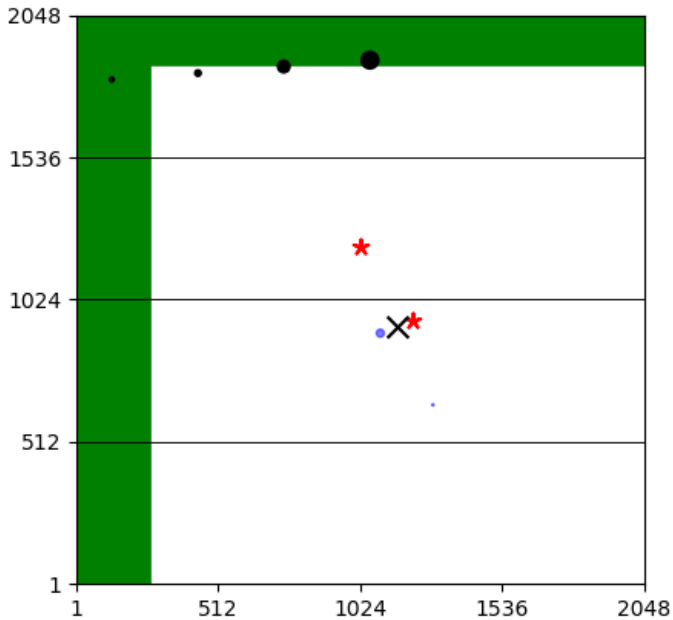

Figure 7-2. Same as Fig. 7-1 but for F115W (CV3).

7.3 F140M

The results for the CV3 measurements in the F140M filter are summarized in Table 7-3 and in Fig. 7-3. A ghost will be observed if the source falls in the region defined by $X \geq 292$ and $Y \leq 1870$.

Table 7-3. Coordinates of the GAP for F140M (CV3)

GAP (*X*, *Y*)	GAP_c (*X*, *Y*)
(1170.0, 934.8)	(1170.2, 929.7)

1. The coordinates of GAP_c are corrected for the geometric distortion.

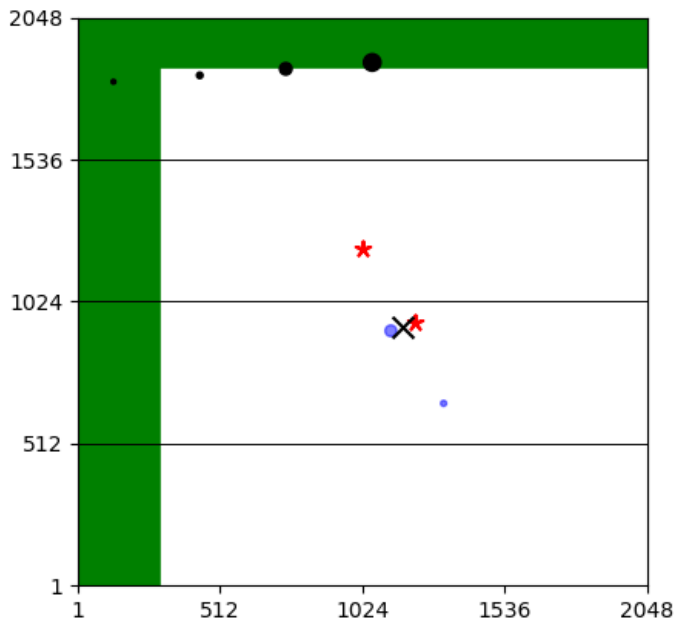

Figure 7-3. Same as Fig. 7-1 but for F140M (CV3).

7.4 F150W

The results for the CV3 measurements in the F150W filter are summarized in Table 7-4 and in Fig. 7-4. A ghost will be observed if the source falls in the region defined by $X \geq 274$ and $Y \leq 1872$.

Table 7-4. Coordinates of the GAP for F150W (CV3)

GAP (X, Y)	GAP_c (X, Y)
(1161.0, 936.1)	(1161.2, 931.1)

1. The coordinates of GAP_c are corrected for the geometric distortion.

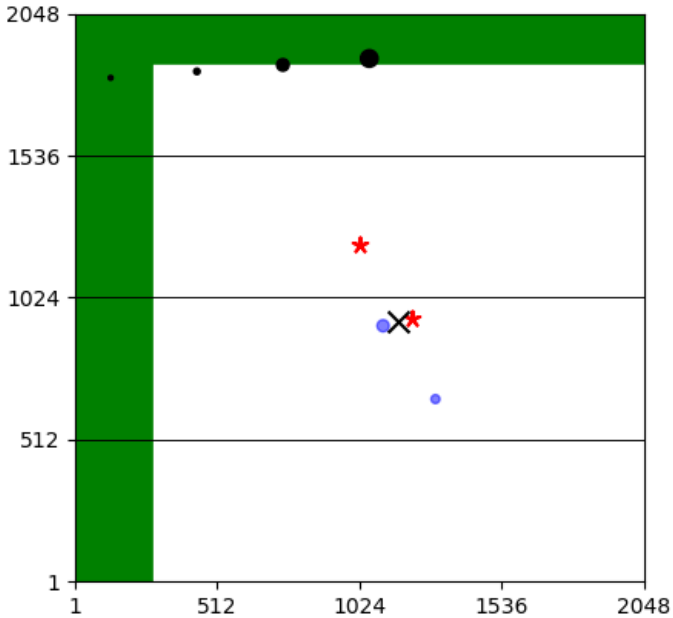

Figure 7-4. Same as Fig. 7-1 but for F150W (CV3).

7.5 F200W

The results for the CV3 measurements in the F200W filter are summarized in Table 7-5 and in Fig. 7-5. A ghost will be observed if the source falls in the region defined by $X \geq 265$ and $Y \leq 1885$. A series of exposures in F200W was also collected as part of OTP 7.21 (and revisions) with the goal of characterizing the PSF-suppression performance of the coronagraphic occulters engraved in the Pick-Off Mirror (Martel 2016). All the OSIM sources were pointed in the upper portion of the detector, inside and immediately outside of the four occulters. Their coordinates mapped a rectangle that spanned the coordinates $X = 125 - 1134$ and $Y = 1750 - 1887$ on the detector. None of the bright PSFs from these tests produced ghosts elsewhere in the FOV, even near the $0.75''$ spot (second from the left). This informs us that either the intensity of the ghosts decreases dramatically away from the GAP, the coordinates of the GAP vary over the FOV thus placing the ghosts outside the FOV, or that the green "exclusion" region is in fact larger than implied by simple geometric considerations. In fact, the CV2 data may support the latter possibility.

Table 7-5. Coordinates of the GAP for F200W (CV3)

GAP (*X*, *Y*)	GAP$_c$ (*X*, *Y*)
(1156.4, 942.7)	(1156.6, 937.7)

1. The coordinates of GAP$_c$ are corrected for the geometric distortion.

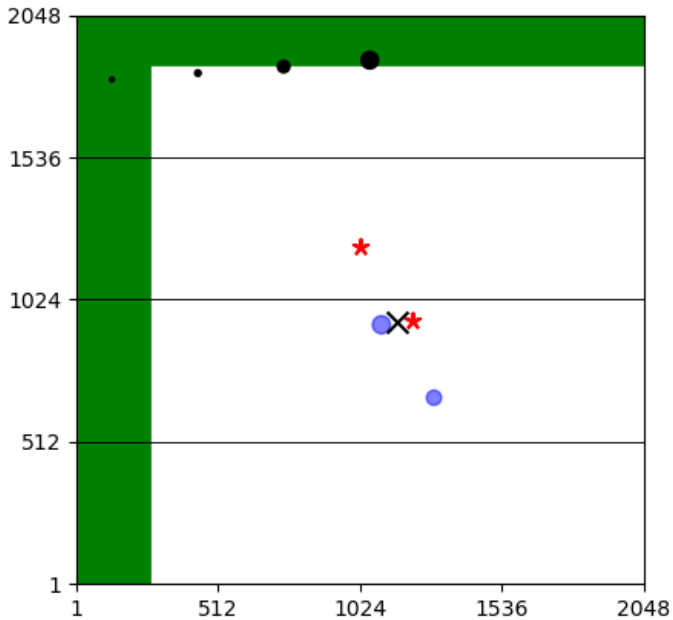

Figure 7-5. Same as Fig. 7-1 but for F200W (CV3).

8 CV2 Campaign

We perform a similar analysis of the ghosts observed in the double-stack filters in the CV2 campaign. The positive identifications are summarized in Table A3-1 in Appendix 3. The coordinates of the OSIM PSFs, ghosts, and GAP, as well as the ghost/source count ratios are tabulated in Tables A3-2 to A3-5. The sources and ghosts are depicted in Figs. A3-1 to A3-4. The high-flux source for F140M was relatively weak (PSF peak of ≈12000 ADUs/pix) and for F158M, barely saturated. Neither produced a detectable ghost, although the GAP of F158M appears to be near the bottom of the FOV and its ghost would not have been detected irrespective of its flux (Section 9; CV1RR). Because the CV2 and CV1RR exposures were collected with a non-flight detector with a slightly different shim than the flight detector installed between the CV2 and CV3 campaigns, we put less emphasis on the results of these two early campaigns.

In CV2, an attempt was made to map the location of the ghosts over the FOV by positioning the bright OSIM source near the field center as well as in the four quadrants. But the ghosts were only detected for the center position. The PSFs, ghosts, and GAPs are plotted in Fig. 8-1 at this central pointing for all four filters.

The non-detection of ghosts when the bright source was pointed in the four quadrants through the double-stack filters may be evidence that the ghost-producing region is in fact smaller and more centrally confined than the region defined solely by the coordinates of the GAP. The light green region in Fig. 8-1 is defined by the four CV2 quadrant pointings and we simply assume that they delineate a rectangle outside of which a bright PSF will not produce a ghost in the FOV. The ghost-producing rectangle therefore spans $305 \leq X \leq 1815$ and $305 \leq Y \leq 1751$. Obviously, a more thorough mapping is required to refine its borders. In this figure, the dark green area is defined by the GAP of F200W.

We now see that the four coronagraphic spots are well contained within the light green area. This may well explain the non-detection of ghosts in OTP 7.21 in F200W in the CV3 campaign. Moreover, in CV1RR, the highly saturated source in the bottom-right quadrant in F115W

(JOBID = 7131) (see Table A4-1) did not produce a ghost at the expected location in the top-left quadrant. This lends further support for a smaller region where bright sources can produce detectable ghosts. Based on the coordinates of this CV1RR PSF, the region may in fact be even more constrained than depicted in Fig. 8-1, $305 \leq X \leq 1687$ and $380 \leq Y \leq 1751$. Two additional saturated PSFs in CV1RR (F140M: JOBID = 7076 and F150W: JOBID = 7057), at the same coordinates of (1504, 1746) in the top-right quadrant also did not produce ghosts. These further constrain the ghost-producing region to about $305 \leq X \leq 1504$ and $380 \leq Y \leq 1746$.

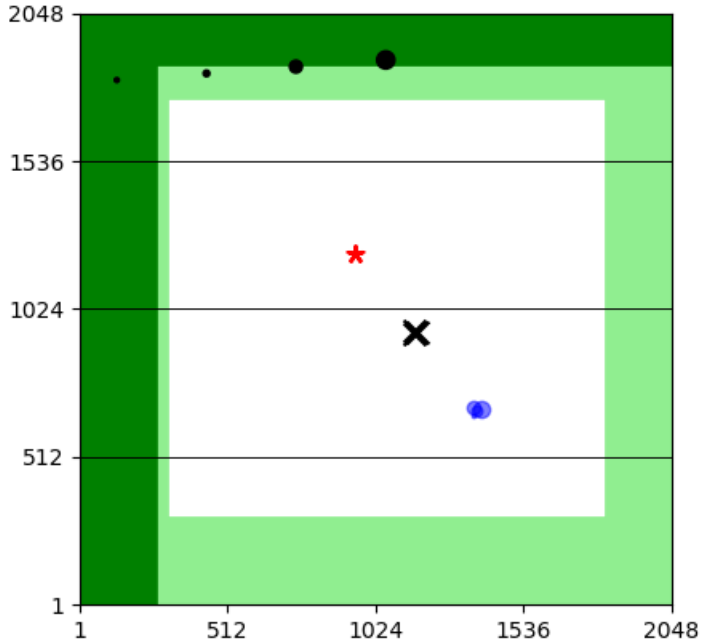

Figure 8-1. The location of the OSIM sources (PSFs; red stars) and their ghosts (blue circles) are plotted for F090W, F115W, F150W, and F200W (CV2). The size of the blue circles correlates with the ghost/source count ratio. The X marks the location of the GAP for each filter. The PSFs overlap completely. Inside the dark green area, a source will not produce a ghost in the FOV as measured from the coordinates of the GAP in F200W. The light green area is defined by the non-detection of ghosts in CV2 when placing a saturated PSF in the four quadrants. The black circles represent the coronagraphic occulters.

9 CV1RR Campaign

For completeness, we examine the imaging ghosts detected in the CV1RR campaign. While the CV2 and CV3 campaigns focused mostly on the ghosts produced by the WFSS blocking filters in the PW, the CV1RR campaign also included elements from the FW. Moreover, the pointing of the OSIM source was different in CV1RR than in those two campaigns, and so this dataset offers additional variety for characterizing the ghosts. Unfortunately, no low-flux PSFs were collected in this campaign so the ratio of the counts between the PSFs and their ghosts cannot be measured.

We find that the coordinates of the GAP for the double-stack filters of the PW (F090W, F115W, and F140M) are consistent with those measured in the OTIS, CV3, and CV2 campaigns, albeit with slight offsets. Obviously, the CV3 and OTIS coordinates have higher priority. The situation for the filters in the FW is more complicated (and confusing). When the OSIM source was pointed near the field center in F380M, F430M, and F480M, all three ghosts appeared very similar and the GAP was also near the center (Fig. A4-4). But when the PSF was moved up by ≈ 350 pixels in F480M, the ghosts appeared near the top edge and the GAP therefore moved up as

well (Fig. A4-5). Hence, we suspect that a reflection off the PAR (Pupil Alignment Reference) in the CLEARP position of the PW is the origin of the common ghosts near the field center for F380M, F430M, and F480M. The optical models by Rohrbach & Irvin (2014) strongly suggest that this is a viable light path. Since both F277W and F480M have the same top GAP, we surmise that the GAPs of the other tilted filters (F356W, F380M, F430M, F444W) in the FW are similar (Hill et al. 2013b).

There may then be two GAPs for the FW, one from a reflection off the PAR when the source is close to the field center (the center GAP) and another from a more common reflection off the tilted filter when the source is off center (the top GAP). There may therefore be a region between the two GAPs where a source will produce two ghosts, one above the top GAP and one below the center GAP. But a close examination of the fields of F277W (JOBID = 7122; Fig. A4-3) and F480M (JOBIDs = 7141 and 7142; Fig. A4-5) that produced ghosts at the top of the FOV does not produce any evidence of a second ghost below the center GAP. The location of the top GAP may explain why no ghost was observed in the F356W exposures in CV3 (Section 7). One possible caveat is that the center GAP is close to the GAP of the PW filters, implying that both wheels may share a common light path in the instrument for producing ghosts at the field center – the PAR would then play no role.

10 Summary

In Table 10-1, the coordinates of the GAP for the PW filters are tabulated. These were calculated from the mean values of all the CV3 and OTIS identifications except for the single-stack filter F158M, which was measured in CV1RR. The coordinates of the GAP for four of the double-stack filters are generally consistent between these two campaigns (at least within the measurement uncertainties). Similarly, in Table 10-2, the location of the two possible GAPs is listed for some of the single-stack filters of the FW – these were available only in the CV1RR campaign. The uncertainties on these coordinates is probably about 2 pix in each axis. A visual representation of all the sources, ghosts, and GAPs presented in this report is provided in Figs. 10-1 (PW) and 10-2 (FW).

Table 10-1. Coordinates of the GAP for the PW Filters

Filter	GAP (*X*, *Y*)	GAP_c (*X*, *Y*)
F090W	(1168.2, 937.6)	(1168.4, 932.5)
F115W	(1151.8, 927.7)	(1152.0, 922.7)
F150W	(1161.4, 936.7)	(1161.6, 931.7)
F200W	(1156.4, 943.8)	(1156.6, 938.8)
F140M	(1170.0, 934.8)	(1170.2, 929.7)
F158M	(1148.0, 314.0)	(1148.2, 309.2)

1. The coordinates of GAP_c are corrected for the geometric distortion.

Table 10-2. Coordinates of the GAP for the FW Filters

Filter	GAP1 (*X*, *Y*)	$GAP1_c$ (*X*, *Y*)	GAP2 (*X*, *Y*)	$GAP2_c$ (*X*, *Y*)
F277W	(1195.5, 1604.5)	(1195.7, 1599.3)	–	–

F480M	(1194.2, 1607.0)	(1194.4, 1601.8)	–	–
F380M	–	–	(1165.0, 949.5)	(1165.2, 944.4)
F430M	–	–	(1165.0, 949.5)	(1165.2, 944.4)
F480M	–	–	(1165.0, 950.5)	(1165.2, 945.4)

1. The coordinates of GAP_c are corrected for the geometric distortion.

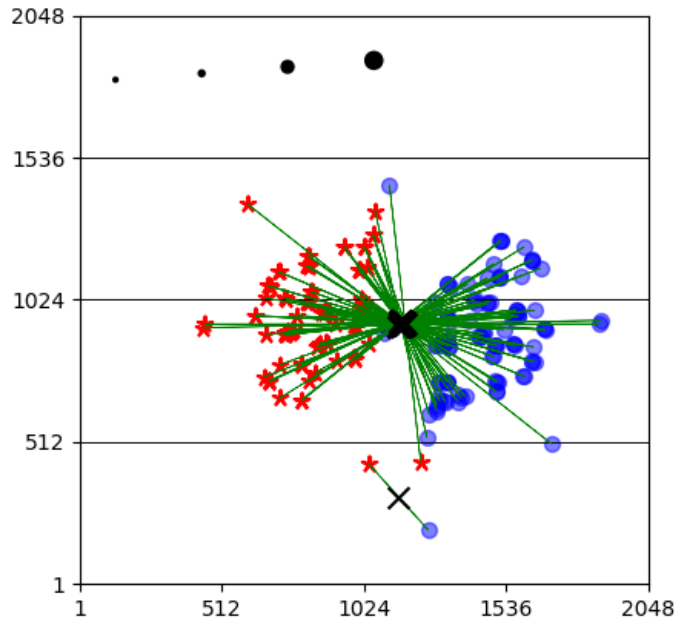

Figure 10-1. The location of all the sources (red stars) that produced ghosts (blue circles) are plotted for the six filters of the PW. They are connected with a green line. The central X marks the location of the GAP of the double-stack filters while the lower X shows the GAP of the single-stack filter F158M. The black circles represent the coronagraphic occulters.

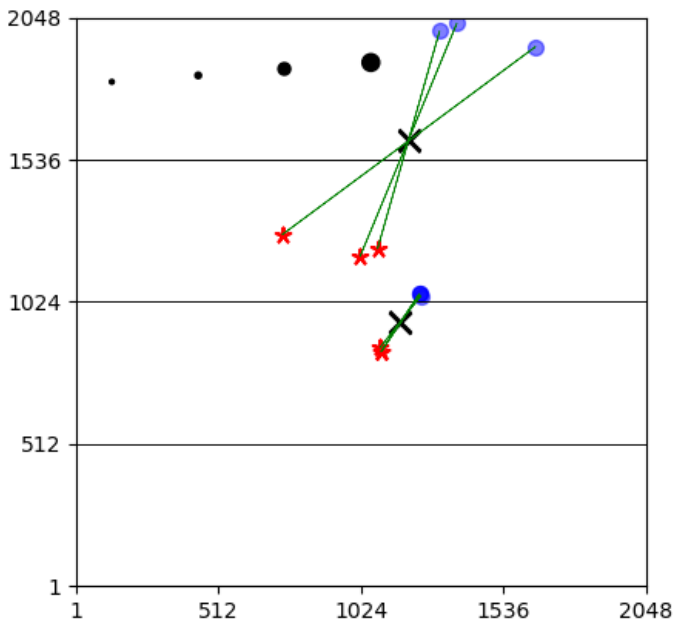

Figure 10-2. Same as Fig. 10-1 but for the FW. GAP2 near the center was measured from F380M, F430M, and F480M (Fig. A4-4) and GAP1, near the top, from F277W and F480M (Figs. A4-3 and A4-5). The CV1RR exposures in F115W with JOBIDS = 5309 and 5314 are not included.

In the following, we summarize our main results:

1. Ghosts were identified in all the filters of the PW and in four of the six filters of the FW. No ghosts were seen in F356W and F444W because the bright PSF was located too far from the GAP or was not sufficiently bright.
2. The ghosts exhibit a wide range of morphologies: a. extended structures with multiple clumps, b. out-of-focus PSFs, c. single faint clumps, or d. distorted PSFs.
3. The morphology of the ghosts varies over the FOV, even for the same filter.
4. The GAP of the double-stack filters in the PW is located near the field center while the GAP of the single-stack filters is closer to the bottom (F158M) or top (FW filters) of the FOV. The coordinates of the GAP are different for each double-stack filter.
5. There may be a second GAP near the field center for the FW filters.
6. Because the GAP is not at the exact center of the field, there is a region far from the GAP and unique to each filter where a bright source will not produce a ghost in the FOV, i.e., the ghost falls "outside" the FOV. For the double-stack filters, this region is along two abutting edges of the FOV.
7. But in addition to this region, calculated from geometric arguments alone, the double-stack filters may also possess a larger area along the full perimeter where a source will not produce a ghost.
8. The ratio of the counts between the ghost and its source is difficult to reconcile between the OTIS and CV3 campaigns. Generally, the ratios are significantly larger for the extended sources in OTIS than for the PSFs in CV3, e.g., 25% vs 0.5% for F090W, 3% vs 0.1% for F115W, 0.8% vs 0.5% for F150W, and 1.3% vs 1.2% for F200W. It is possible that the OTIS observations were contaminated by stray light, external reflections, or vignetting from the ASPA source module. A complete model of the sources and their light path is beyond the scope of this report.
9. Although the distribution of the sources is limited and the measurements are difficult and uncertain, the count ratios do not show a convincing radial dependence away from the

GAP, as the optical models predict.

11 Discussion

For the science modes, the imaging ghosts will primarily impact individual direct images interleaved with the GR150C/R exposures of the WFSS mode when prime or parallel, as well as NIRISS images acquired as coordinated or pure parallels. Imaging in the engineering and calibration modes, i.e., the focus sweep, will also be affected. The removal or correction of ghosts in single exposures will prove difficult because their morphology varies over the FOV and between filters. But the majority of the NIRISS modes are implemented with pre-defined dither patterns, which should help eliminate the majority of the ghosts in the combined image if the dither steps are large enough to step over the footprint of the ghosts. This is illustrated in Fig. 11-1. A bright source (red star) is placed at three dither positions separated by an exaggerated offset of 300 pixels horizontally. At the second position, the ghost (blue circle) contaminates a galaxy (pink diamond). After registering and combining the three images, the galaxy will still be contaminated by the ghost. The image of the second position should therefore be excluded from the combination or the pixels subtended by the ghost should be masked out. With a large number of dithers, a simple median combination would remove the ghost. If the dither steps are small, all three ghosts will overlap the galaxy in the final combined image.

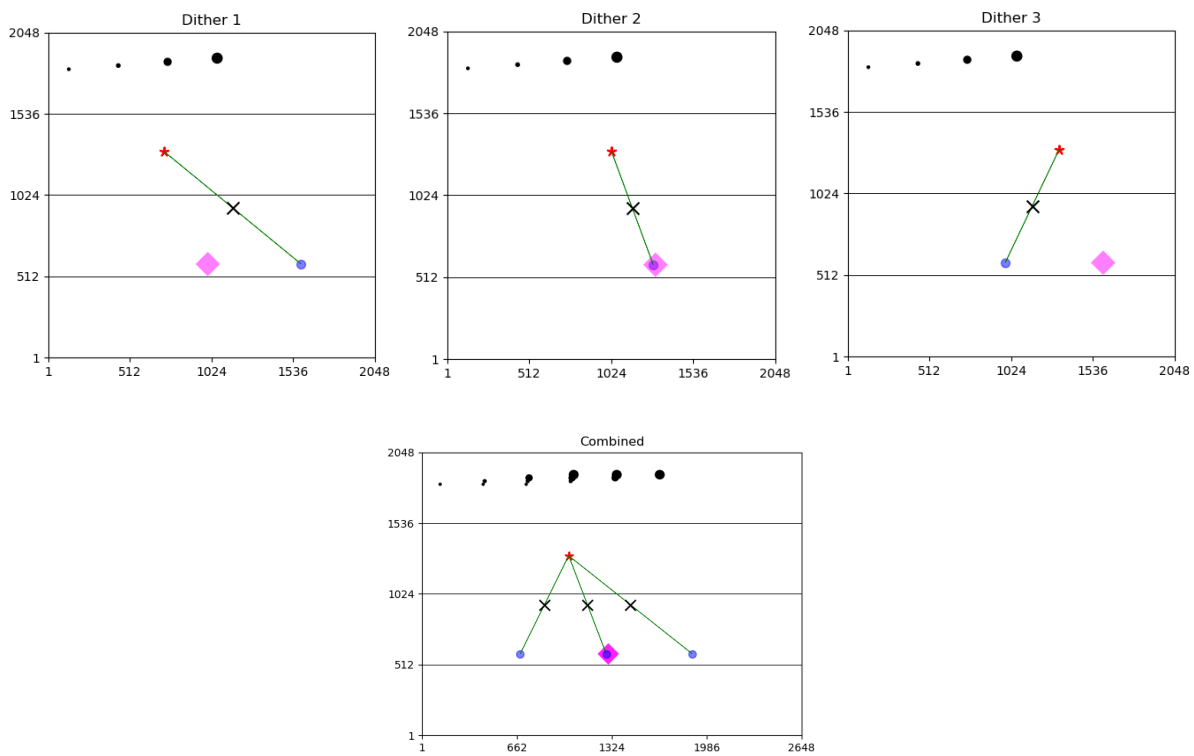

Figure 11-1. In the top panels, a bright star (red star) is dithered by 300 pixels horizontally and its ghost (blue circle) contaminates a galaxy (pink diamond) at the second dither position. In the bottom panel, the images are combined using the second position as the reference image. The black X marks the location of the GAP and the green line connects the source to its ghost.

Achieving an absolute flux calibration at an accuracy of ~1% or better in integrated counts (or ~0.01 mag) will also prove problematic. As we showed above, the ghost of a bright source located far from its GAP will fall outside the FOV and so is not available to correct the photometry. The flux calibration would therefore need to be derived from flux standard stars placed nearer to the GAP. A comprehensive calibration will necessitate placing the calibrator

star(s) in regions where the ghost can be detected and where it can not and comparing their photometry. The target would also need to be imaged up to full well saturation to accumulate a sufficient number of counts in the ghost for a reliable analysis. The observations should be dithered so information can be extracted from the single and combined images. The choice of appropriate flux standards for this calibration is likely limited because these bright stars quickly saturate in most NIRISS bandpasses. Alternatively, one could simply make use of field stars with a variety of brightnesses and field locations. Lastly, we note that F158M is a reasonable choice for the NIRISS on-orbit focus sweep with its Coarse Focus Mechanism (CFM) since its GAP is near the edge of the FOV and so the number of ghosts in this potentially crowded star field will be minimized.

12 Conclusion

We have identified several examples of optical imaging ghosts in full-frame exposures collected over several years in the ground cryo campaigns at GSFC and JSC. This comprehensive collection will serve as a baseline for the identification of ghosts in the early on-orbit commissioning activities. Eventually, the morphology, location, and contribution of the ghosts will be updated as a variety of astronomical sources are imaged during the on-orbit lifetime of NIRISS. After improving the coordinates of the GAP of each filter, it should become straightforward to separate the ghosts from true astronomical sources.

13 References

Aldridge et al. 2011, 4B Optical Sub-Assembly Design; CDR Oct 19 – 20, 2011

Cox, C., Lallo, M., van der Marel, R.P., & Donaldson, T. 2008, Description and Use of the JWST Science Instrument Aperture File, JWST-STScI-001550 (Baltimore: STScI)

Davila, P.S. et al. 2008, The Optical Telescope Element Simulator for the James Webb Space Telescope, in Space Telescopes and Instrumentation, Edited by J.M. Oschmann Jr., M.W.M. de Graauw, and H.A. MacEwen, Proceedings of the SPIE, Vol. 7010

Hill, P. et al. 2013a, NIRISS and FGS Stray Light Findings (Based on the ISIM FRED Model) (slide package; ITAR)

Hill, P. et al. 2013b, NIRISS Focus w.r.t. Filter Curvature and Preliminary GR150 Ghosting Analysis (Based on the ISIM FRED Model) (slide package; ITAR)

Martel, A.R. et al. 2014, Inputs to the NIRISS Performance Verification in the CV2 ISIM Campaign, JWST-STScI-003850 (Baltimore: STScI)

Martel, A.R. et al. 2016, Inputs to the NIRISS Performance Verification in the ISIM CV3 Campaign, JWST-STScI-004354 (Baltimore: STScI)

Martel, A.R. 2016, Analysis of NIRISS CV3 Data: PSF Suppression with the Coronagraphic Occulters, JWST-STScI-0050302 (Baltimore: STScI)

Martel, A., & Fullerton, A. 2016, The Geometric Distortion of NIRISS, JWST-STScI-003524 (Baltimore: STScI)

Miskey, C. 2014, Test Planning Tool User's Guide, Version 2, JWST-HDBK-024894 (Jul 30, 2014)

Rohrbach, S. & Irvin, R. 2014, NIRISS CV1RR Ghost Diagnosis of Imaging and WFSS Modes (slide package; ITAR)

Sullivan, J. et al. 2010, Manufacturing and Integration Status of the JWST OSIM Optical Simulator, in Space Telescopes and Instrumentation, Edited by J.M. Oschmann Jr., M.C. Clampin, and H.A. MacEwen, Proceedings of the SPIE, Vol. 7731

Appendix 1
OTIS Campaign Data

A catalogue of the exposures with ghosts is presented in Table A1-1. They were collected at the cold plateau (Focal Plane Assembly (FPA) temperature of 37.4 – 38.0K) except for JOBIDs = 542 and 546 which were taken at 67K during the cooldown. The activities are identified by their OTP numbers. The broad-band (O-13) or monochromatic (O-1 and O-22) outward (1.5 Pass) ASPA sources were selected with a pulsed (p) or continuous (c) illumination. Except for OTP 7.22 and 7.22a NIRISS Grism and Imaging Checkout, background exposures that matched the DW combination and number of groups of the source exposures were also acquired. For completeness, we note that JOBIDs = 789, 793, and 1004 possess ghosts but they are too faint to reliably measure their properties.

Table A1-1. Catalogue of the ASPA Sources (OTIS)

PW	FW	OTP	JOBID	ASPA Source[2]
F090W	CLEAR	7.22	2867	O-13 (c)
		7.22a	2891	O-13 (c)
F115W	CLEAR	7.22	2868	O-13 (c)
		7.22a	2888	O-13 (c)
F150W	CLEAR	312.9.6	542, 546[1]	O-22 1.55 μm (p)
		312.9.6 Rev A	783, 787	O-22 1.55 μm (p)
			796	O-22 1.55 μm (c)
		312.9.5 Rev G	1005, 1007	O-22 1.55 μm (p)
		3810.1 Rev A	2573	O-1 1.55 μm (c)
F200W	CLEAR	323.3.1	3727	O-1 2.12 μm (c)
		323.3 Rev A	3792	O-1 2.12 μm (c)
		323.3 Rev B	3842, 3843	O-1 2.12 μm (p)

1. These two exposures, collected at 67K during the cooldown, possess a large population of hot pixels that don't subtract completely with the background correction.
2. The illumination from the ASPA sources is either continuous (c) or pulsed (p).

In Tables A1-2 to A1-17, we tabulate the centroid of the sources and their corresponding ghosts as well as the ratio of their counts. In some exposures, one or two ghosts were too faint to measure accurately. We show some representative full-frame images in Figs. A1-1 to A1-8. The sources and ghosts in the other exposures of Table A1-1 are very similar and so we don't display them. The brightest blobs in the sources typically have peak counts of 2000 – 30000 ADUs/pix and so are not saturated. But we exclude JOBID = 1006 which is saturated (59000 ADUs/pix).

A1.1 F090W

Table A1-2. Sources and Ghosts in JOBID = 2867 (F090W)

Number	Source (X, Y)	Ghost (X, Y)	GAP (X, Y)	Ratio (%)
1	(1009.5, 994.3)	(1324.8, 879.8)	(1167.2, 937.1)	22

Table A1-3. Sources and Ghosts in JOBID = 2891 (F090W)

Number	Source (*X*, *Y*)	Ghost (*X*, *Y*)	GAP (*X*, *Y*)	Ratio (%)
1	(1013.8, 997.6)	(1321.0, 882.4)	(1167.4, 940.0)	28

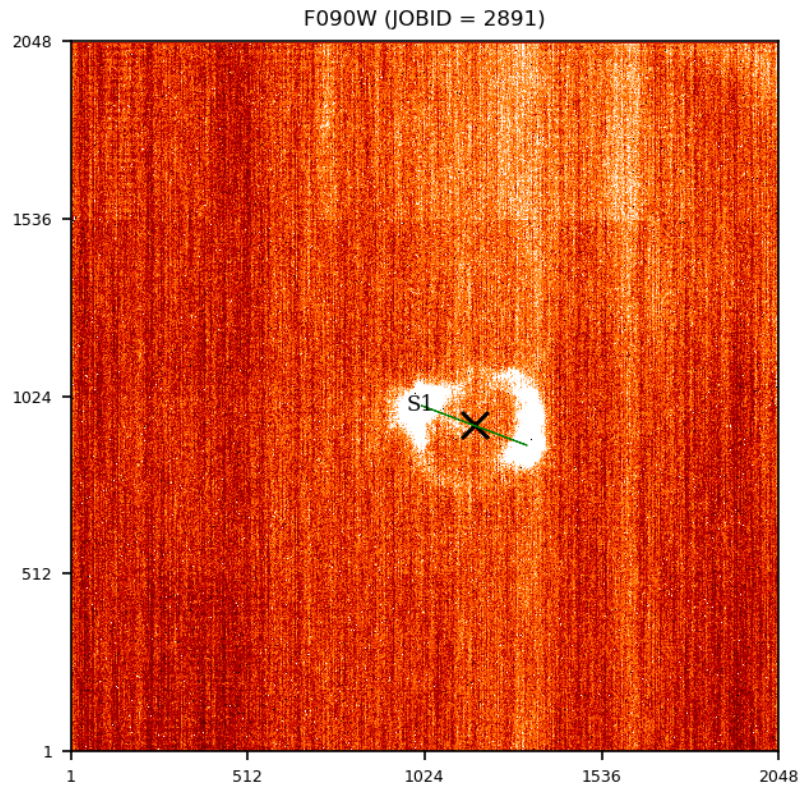

Figure A1-1. The bright ASPA source for JOBID = 2891 (F090W) is labelled S1. It is connected to its ghost by the green line. The black X near the field center marks the location of the GAP.

A1.2 F115W

Table A1-4. Sources and Ghosts in JOBID = 2868 (F115W)

Number	Source (*X*, *Y*)	Ghost (*X*, *Y*)	GAP (*X*, *Y*)	Ratio (%)
1	(1011.5, 993.2)	(1284.8, 861.3)	(1148.2, 927.2)	2.4

Table A1-5. Sources and Ghosts in JOBID = 2888 (F115W)

Number	Source (*X*, *Y*)	Ghost (*X*, *Y*)	GAP (*X*, *Y*)	Ratio (%)
1	(1017.6, 996.2)	(1280.4, 858.6)	(1149.0, 927.4)	4.0

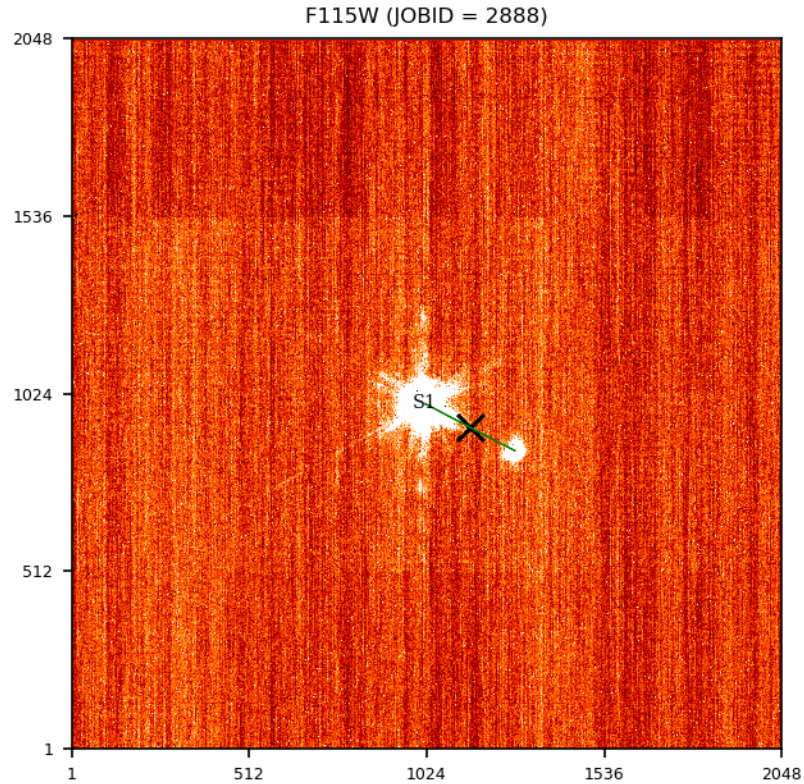

Figure A1-2. Same as Fig. A1-1 but for source S1 of JOBID = 2888 (F115W).

A1.3 F150W

Table A1-6. Sources and Ghosts in JOBID = 542 (F150W)

Number	Source (*X*, *Y*)	Ghost (*X*, *Y*)	GAP (*X*, *Y*)	Ratio (%)
1	(1023.4, 1011.4)	(1303.6, 865.6)	(1163.5, 938.5)	0.76
2	–	–	–	–
3	(1035.8, 1139.8)	(1292.7, 728.8)	(1164.2, 934.3)	0.78
4	(835.0, 1052.9)	(1486.0, 821.6)	(1160.5, 937.2)	0.76
5	(721.3, 1123.8)	(1597.1, 748.6)	(1159.2, 936.2)	0.69
6	(824.7, 1181.6)	(1499.0, 694.7)	(1161.8, 938.2)	0.46
7	–	–	–	–
8	(750.2, 911.8)	(1578.8, 964.0)	(1164.5, 937.9)	0.72
9	(894.9, 982.7)	(1433.9, 893.7)	(1164.4, 938.2)	0.47
			(1162.6 ± 2.7, 937.2 ± 1.4)	

Table A1-7. Sources and Ghosts in JOBID = 546 (F150W)

Number	Source (*X*, *Y*)	Ghost (*X*, *Y*)	GAP (*X*, *Y*)	Ratio (%)
1	(1022.6, 1013.1)	(1305.1, 863.2)	(1163.8, 938.2)	0.91

2	–	–	–	–
3	(1035.4, 1141.4)	(1293.6, 727.0)	(1164.5, 934.2)	0.87
4	(831.5, 1053.8)	(1489.3, 820.5)	(1160.4, 937.1)	0.97
5	(714.1, 1125.7)	(1602.6, 747.2)	(1158.4, 936.4)	0.92
6	(821.9, 1182.2)	(1502.4, 693.9)	(1162.1, 938.0)	0.61
7	–	–	–	–
8	(747.3, 911.1)	(1580.0, 965.8)	(1163.6, 938.5)	0.85
9	(888.1, 985.2)	(1441.0, 890.5)	(1164.6, 937.8)	0.71
			(1162.5 ± 2.2, 937.2 ± 1.4)	

Table A1-8. Sources and Ghosts in JOBID = 783 (F150W)

Number	Source (*X*, *Y*)	Ghost (*X*, *Y*)	GAP (*X*, *Y*)	Ratio (%)
1	(1019.6, 1010.3)	(1305.6, 867.0)	(1162.6, 938.6)	0.78
2	–	–	–	–
3	(1004.7, 1133.5)	(1326.0, 728.9)	(1165.4, 931.2)	0.27
4	(824.8, 1013.4)	(1492.5, 862.2)	(1158.7, 937.8)	1.0
5	(686.5, 1072.4)	(1627.7, 803.3)	(1157.1, 937.8)	0.86
6	(824.1, 1145.4)	(1494.5, 732.1)	(1159.3, 938.7)	1.2
7	(862.2, 866.4)	(1465.7, 1008.2)	(1163.9, 937.3)	0.71
8	(767.8, 916.2)	(1555.4, 959.6)	(1161.6, 937.9)	0.70
9	(880.8, 982.5)	(1444.4, 892.6)	(1162.6, 937.5)	0.65
			(1161.4 ± 2.6, 937.1 ± 2.3)	

Table A1-9. Sources and Ghosts in JOBID = 787 (F150W)

Number	Source (*X*, *Y*)	Ghost (*X*, *Y*)	GAP (*X*, *Y*)	Ratio (%)
1	(1018.3, 1007.6)	(1308.0, 869.1)	(1163.2, 938.4)	1.1
2	–	–	–	–
3	(1006.5, 1132.1)	(1324.2, 728.5)	(1165.3, 930.3)	0.38
4	(813.3, 1015.4)	(1503.3, 860.6)	(1158.3, 938.0)	1.2
5	(674.4, 1074.8)	(1638.0, 802.0)	(1156.2, 938.4)	0.80
6	(812.8, 1147.3)	(1505.0, 730.2)	(1158.9, 938.8)	1.3
7	(851.2, 855.9)	(1477.9, 1018.4)	(1164.5, 937.1)	0.80
8	(756.9, 907.1)	(1568.5, 970.4)	(1162.7, 938.8)	0.83
9	(869.2, 974.3)	(1457.8, 902.6)	(1163.5, 938.5)	0.89
			(1161.6 ± 3.1, 937.3 ± 2.7)	

Table A1-10. Sources and Ghosts in JOBID = 796 (F150W)

Number	Source (*X*, *Y*)	Ghost (*X*, *Y*)	GAP (*X*, *Y*)	Ratio (%)
1	(1023.5, 1007.1)	(1302.4, 869.3)	(1162.9, 938.2)	1.0
2	–	–	–	–
3	(1008.4, 1131.7)	(1322.9, 728.5)	(1165.7, 930.1)	0.36
4	(821.3, 1014.9)	(1497.4, 860.7)	(1159.3, 937.8)	1.0
5	(683.7, 1073.9)	(1630.1, 801.7)	(1156.9, 937.8)	0.91
6	(819.9, 1147.1)	(1500.4, 729.8)	(1160.2, 938.5)	0.99
7	(858.8, 858.2)	(1468.0, 1017.7)	(1163.4, 937.9)	0.86
8	(765.7, 908.7)	(1559.8, 968.3)	(1162.8, 938.5)	0.80
9	(878.3, 974.7)	(1448.4, 903.0)	(1163.3, 938.8)	0.75
			(1161.8 ± 2.6, 937.2 ± 2.7)	

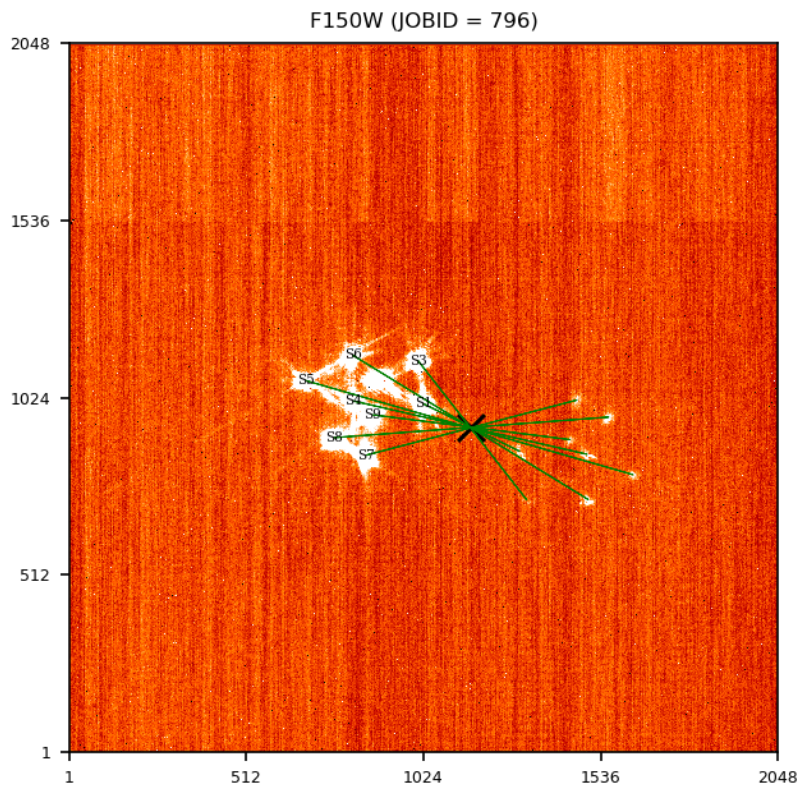

Figure A1-3. Same as Fig. A1-1 but for the multiple sources S1 to S9 of JOBID = 796 (F150W).

Table A1-11. Sources and Ghosts in JOBID = 1005 (F150W)

Number	Source (*X*, *Y*)	Ghost (*X*, *Y*)	GAP (*X*, *Y*)	Ratio (%)
1	(443.8, 924.2)	(1877.2, 950.1)	(1160.5, 937.1)	0.44

Table A1-12. Sources and Ghosts in JOBID = 1007 (F150W)

Number	Source (*X*, *Y*)	Ghost (*X*, *Y*)	GAP (*X*, *Y*)	Ratio (%)
1	(450.4, 936.8)	(1871.1, 937.5)	(1160.8, 937.1)	0.53

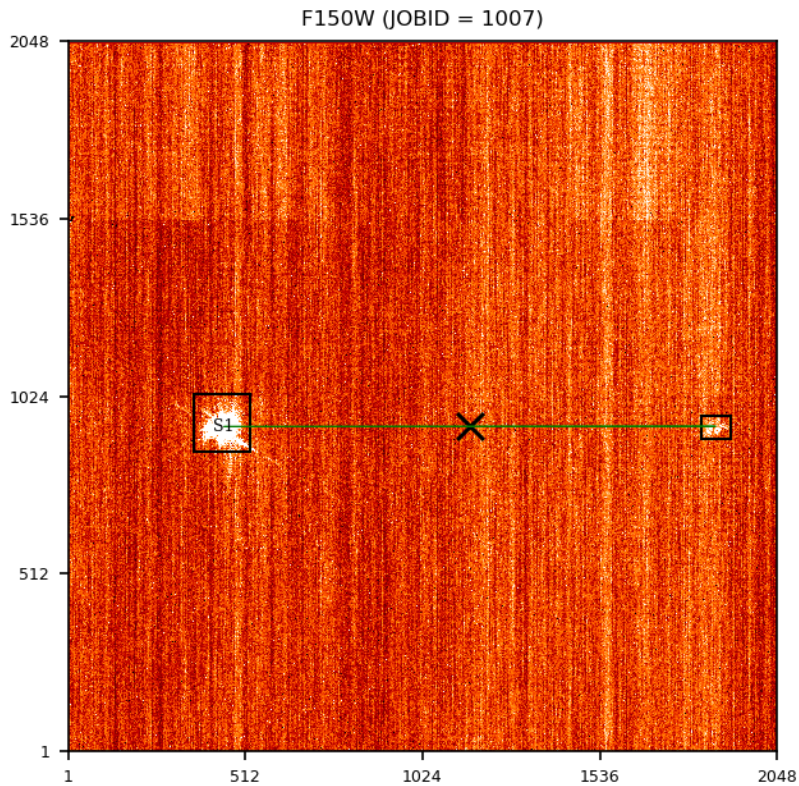

Figure A1-4. Same as Fig. A1-1 but for source S1 of JOBID = 1007 (F150W). The black boxes delimit the regions around the source and its ghost that were used to calculate their integrated counts.

Table A1-13. Sources and Ghosts in JOBID = 2573 (F150W)

Number	Source (*X*, *Y*)	Ghost (*X*, *Y*)	GAP (*X*, *Y*)	Ratio (%)
1	(662.0, 745.1)	(1659.2, 1137.4)	(1160.6, 941.3)	1.3

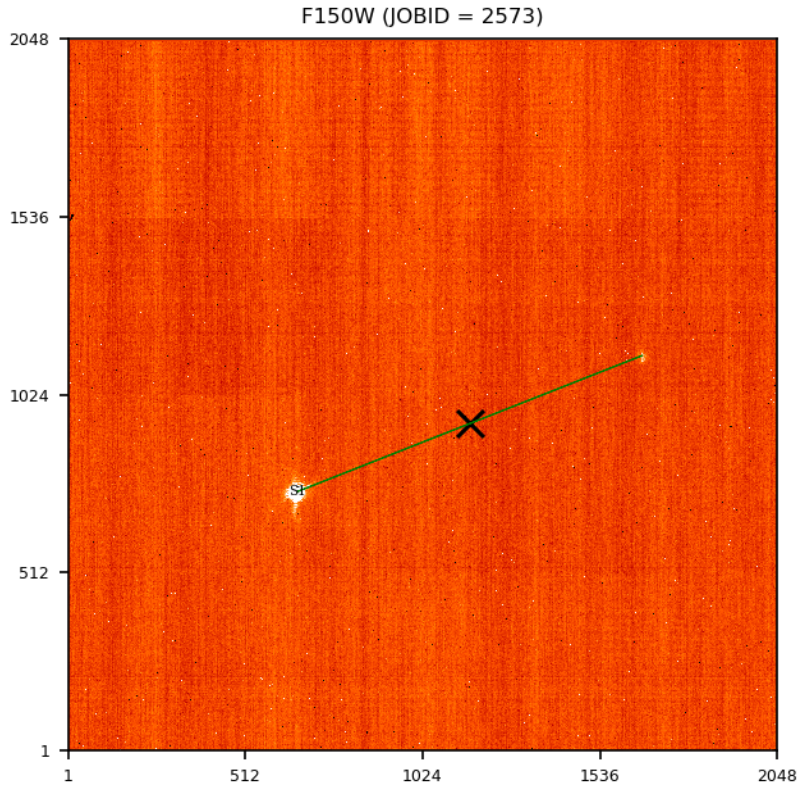

Figure A1-5. Same as Fig. A1-1 but for source S1 of JOBID = 2573 (F150W).

A1.4 F200W

Table A1-14. Sources and Ghosts in JOBID = 3727 (F200W)

Number	Source (*X*, *Y*)	Ghost (*X*, *Y*)	GAP (*X*, *Y*)	Ratio (%)
1	(1039.7, 868.8)	(1278.6, 1015.9)	(1159.1, 942.3)	1.1
2	(924.2, 803.3)	(1396.6, 1081.2)	(1160.4, 942.2)	0.76
3	(921.4, 940.3)	(1401.3, 949.9)	(1161.3, 945.1)	1.0
4	(782.6, 967.5)	(1527.3, 916.2)	(1155.0, 941.8)	0.83
5	(670.3, 899.9)	(1638.4, 985.7)	(1154.4, 942.8)	0.82
6	(670.2, 1030.8)	(1634.5, 853.9)	(1152.4, 942.4)	1.8
7	(826.7, 731.0)	(1490.3, 1153.3)	(1158.5, 942.1)	0.67
8	(718.5, 669.5)	(1600.6, 1214.8)	(1159.6, 942.2)	0.55
9	(721.9, 790.5)	(1587.8, 1110.6)	(1154.8, 950.6)	1.7
			(1157.3 ± 3.0, 943.5 ± 2.7)	

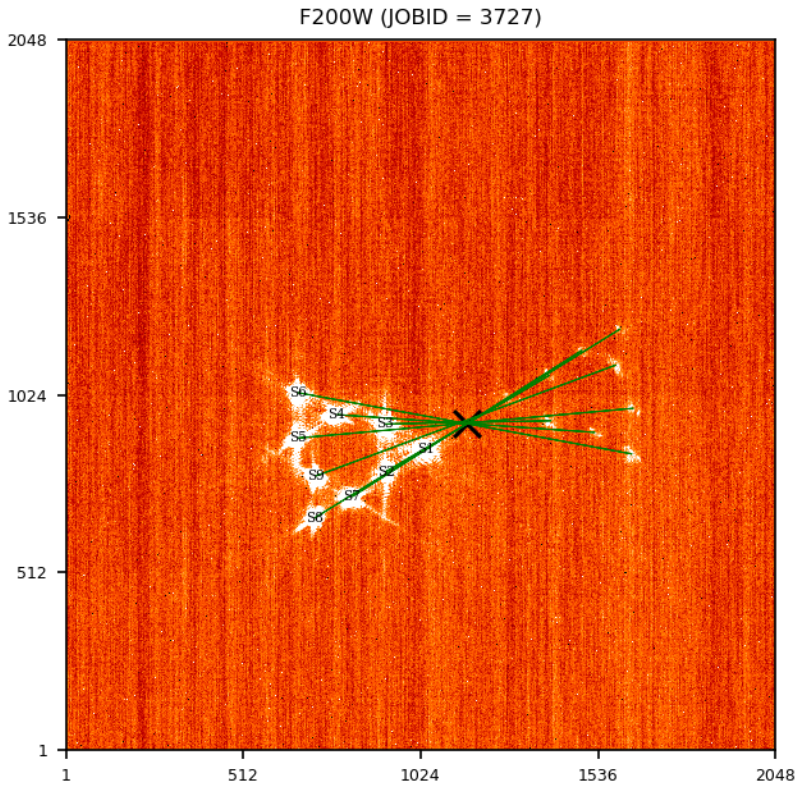

Figure A1-6. Same as Fig. A1-1 but for sources S1 to S9 of JOBID = 3727 (F200W).

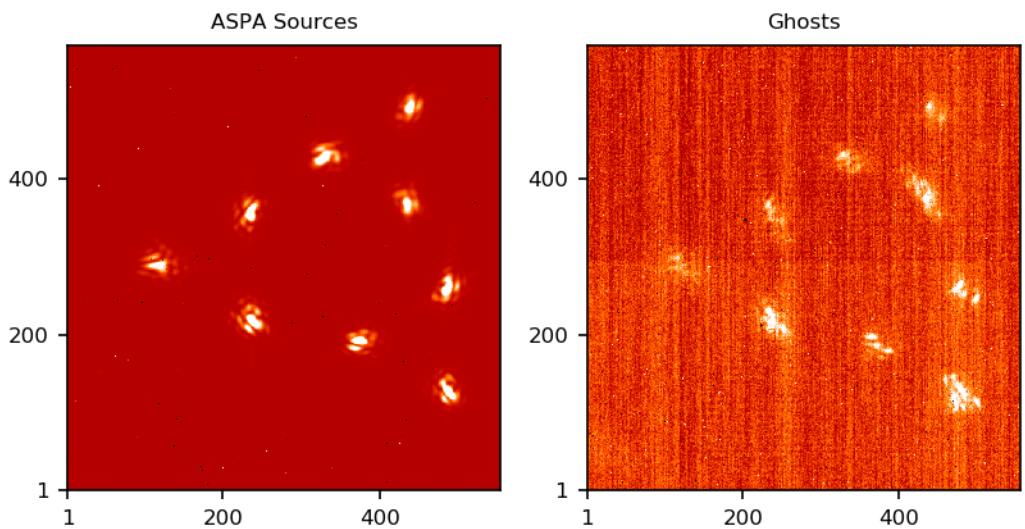

Figure A1-7. Enlargement of the ASPA sources rotated by 180° (left) and their associated ghosts (right) for JOBID = 3727. Both the sources and their ghosts possess clumpy morphologies that do not overlap.

Table A1-15. Sources and Ghosts in JOBID = 3792 (F200W)

Number	Source (*X*, *Y*)	Ghost (*X*, *Y*)	GAP (*X*, *Y*)	Ratio (%)
1	(986.6, 817.0)	(1333.4, 1069.7)	(1160.0, 943.3)	0.90
2	(885.1, 873.8)	(1426.4, 1011.7)	(1155.8, 942.8)	0.77

Number	Source (*X*, *Y*)	Ghost (*X*, *Y*)	GAP (*X*, *Y*)	Ratio (%)
3	(988.0, 934.2)	(1332.2, 950.2)	(1160.1, 942.2)	0.98
4	(734.2, 902.2)	(1579.0, 980.0)	(1156.6, 941.0)	0.70
5	(631.2, 967.6)	(1676.2, 915.0)	(1153.7, 941.3)	0.59
6	(738.8, 1029.8)	(1567.7, 860.0)	(1153.2, 944.9)	1.2
7	(799.2, 660.7)	(1513.8, 1237.8)	(1156.5, 949.3)	1.7
8	(682.1, 729.0)	(1629.1, 1168.2)	(1155.6, 948.6)	2.4
9	(798.8, 789.5)	(1511.6, 1108.2)	(1155.2, 948.8)	1.8
			(1156.3 ± 2.3, 944.7 ± 3.2)	

Table A1-16. Sources and Ghosts in JOBID = 3842 (F200W)

Number	Source (*X*, *Y*)	Ghost (*X*, *Y*)	GAP (*X*, *Y*)	Ratio (%)
1	(993.6, 808.7)	(1322.9, 1083.4)	(1158.2, 946.0)	1.3
2	(891.1, 864.9)	(1420.3, 1022.2)	(1155.7, 943.6)	0.96
3	(995.7, 926.2)	(1324.2, 960.4)	(1159.9, 943.3)	1.3
4	(739.2, 897.5)	(1572.8, 988.0)	(1156.0, 942.7)	0.87
5	(632.1, 965.4)	(1672.5, 919.0)	(1152.3, 942.2)	0.74
6	(743.7, 1025.2)	(1563.9, 865.0)	(1153.8, 945.1)	1.3
7	(798.7, 663.6)	(1515.6, 1236.2)	(1157.2, 949.9)	1.8
8	(681.5, 731.8)	(1628.0, 1166.7)	(1154.7, 949.3)	2.5
9	(798.3, 792.2)	(1513.2, 1106.7)	(1155.8, 949.4)	2.1
			(1156.0 ± 2.2, 945.7 ± 2.9)	

Table A1-17. Sources and Ghosts in JOBID = 3843 (F200W)

Number	Source (*X*, *Y*)	Ghost (*X*, *Y*)	GAP (*X*, *Y*)	Ratio (%)
1	(993.7, 808.4)	(1323.2, 1083.7)	(1158.5, 946.0)	1.5
2	(890.7, 864.7)	(1420.9, 1024.0)	(1155.8, 944.3)	0.97
3	(995.3, 925.8)	(1324.0, 960.6)	(1159.6, 943.2)	1.2
4	(739.6, 897.2)	(1571.6, 988.0)	(1155.6, 942.6)	0.80
5	(632.6, 965.4)	(1672.3, 918.8)	(1152.4, 942.1)	0.69
6	(744.0, 1025.0)	(1563.5, 865.3)	(1153.7, 945.2)	1.2
7	(799.4, 663.8)	(1514.7, 1235.6)	(1157.0, 949.7)	1.9
8	(681.7, 732.2)	(1628.2, 1166.4)	(1154.9, 949.3)	2.6
9	(798.7, 792.3)	(1513.1, 1106.3)	(1155.9, 949.3)	2.1

Number	Source (*X*, *Y*)	Ghost (*X*, *Y*)	GAP (*X*, *Y*)	Ratio (%)
			(1155.9 ± 2.1, 945.7 ± 2.8)	

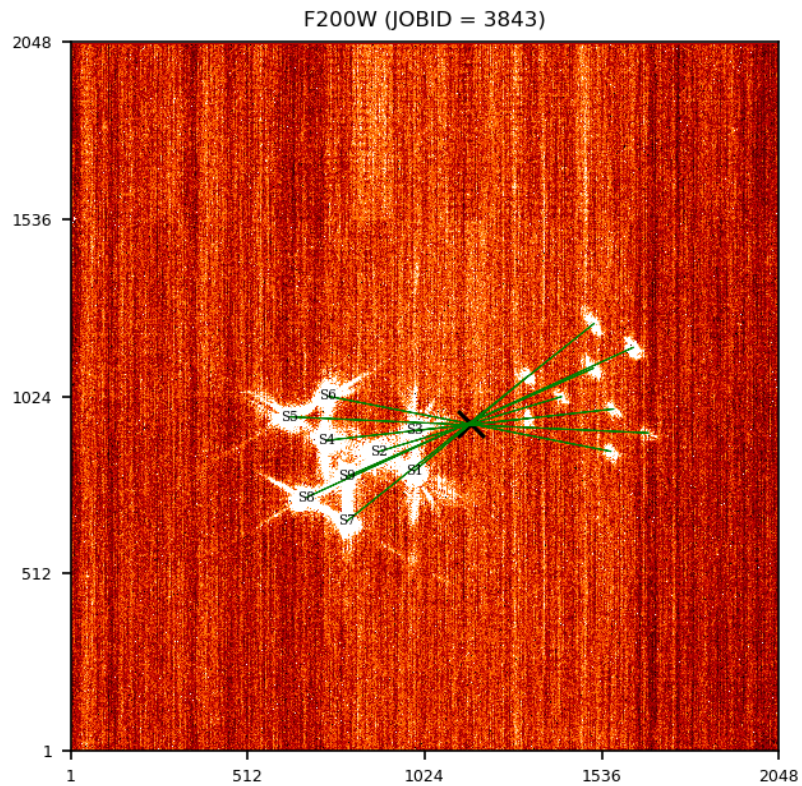

Figure A1-8. Same as Fig. A1-1 but for sources S1 to S9 of JOBID = 3843 (F200W).

Appendix 2
CV3 Campaign Data

A catalogue of the exposures that produced ghosts is presented in Table A2-1. The exposures were collected in a series of activities in CV3 at the cold plateau of 37.7K (Martel et al. 2016). The configuration of NIRISS and the OTE Simulator (OSIM; Davila et al. 2008; Sullivan et al. 2010) were commanded with state tables generated with the TPT (Miskey 2014). NIRISS was at its best focus of $+0.1$ OTE mm except for the first-light tests OTP 0.2.1.1.NR Rev A and OTP 0.2.4.1.NR for which the focus was at -0.2 and $+0.4$ OTE mm, respectively. A significant number of exposures were taken as part of the characterization of the WFSS grisms (GR150C/R) in OTP 7.6.*. Hence the catalogue is heavily biased towards the blue filters of the PW. The OSIM source was pointed at the same location for the all filters. Each exposure consisted of a single integration.

In CV3, OSIM could deliver one of five sources through the NIRISS light path: a broad-band tungsten source (TUNG) and four monochromatic sources (0.64, 1.06, 1.32, and 1.55 μm) for the wavelength calibration of the grisms. The combination of source temperature, attenuation, and number of groups in TPT usually constrained the range of fluxes that could be explored. For the majority of observations, we selected a continuous illumination but in a few cases, the source had to be pulsed to avoid saturation in the first or second group. For a given DW configuration, the source was held at a constant temperature and commanded at two flux levels at the same pixel position in consecutive exposures: a low flux source, which produced an unsaturated PSF, followed by a high flux source that produced a saturated PSF and in some cases, ghosts somewhere in the FOV. After examining all the exposures carefully, we find that only some exposures illuminated with the TUNG source produced ghosts – the flux in the monochromatic PSFs was insufficient. The lamp temperature was typically $1000-1500$K and the flux ratios $7-105$. Background exposures that matched the DW combination and number of groups of the source exposures were also acquired.

Table A2-1. Catalogue of Low- and High-Flux OSIM Sources (CV3)

PW	FW	OTP	OSIM Source[1]	JOBID[2]
F090W	CLEAR	7.6.1	TUNG (p)	35745, 35747
			TUNG (p)	35749, 35754
F115W	CLEAR	7.6.2	TUNG (c)	35795, 35797
			TUNG (c)	35799, 35801
F140M	CLEAR	7.6.4	TUNG (c)	35881, 35882
			TUNG (c)	35883, 35884
F150W	CLEAR	7.6.5	TUNG (c)	35939, 35941
			TUNG (c)	35943, 35945
F200W	CLEAR	7.6.6	TUNG (c)	35991, 35993
			TUNG (c)	35995, 35996

1. The OSIM source is the continuum tungsten source (TUNG). The illumination is either continuous (c) or pulsed (p).
2. The JOBIDs of the exposure with the low-flux PSF (left entry) and of its high-flux counterpart (right entry) are tabulated.

In Tables A2-2 to A2-6, we tabulate the centroid of the sources and their corresponding ghosts, the coordinates of the GAP, as well as the ratio of their counts. As mentioned above, the ratio is

calculated by scaling the total counts in the low-flux PSF to its high-flux counterpart using the TPT scaling factor.

A2.1 F090W

The properties of the source and ghosts are summarized in Table A2-2. In JOBID = 35747, a ghost is observed near the bright PSF (Fig. A2-1). This ghost (≈ 0.74%) consists of a bright knot and a diffuse component to its left. Its diameter is about 20 pixels. At coordinates (1276, 873), a diffuse and weak feature is observed. As we will see below, it is present at the same coordinates in the other filters and is likely a detector defect that is highlighted by the contrast of the PSF wings. In JOBID = 35754 (Fig. A2-2), we observe one ghost far from the PSF. It possesses a clear spiral morphology – the two faint arms are at the top and bottom of the bright core. The diameter of this ghost is also about 20 pixels.

These observations demonstrate that some features of the ghosts possess a strong field dependence. The bright OSIM source was displaced by only 325 pixels near the center of the field between the exposures and yet the location and morphology of their ghosts vary considerably.

Table A2-2. Sources and Ghosts for F090W (CV3)

JOBID	Number	Source (*X*, *Y*)	Ghost (*X*, *Y*)	GAP (*X*, *Y*)	Ratio[1] (%)
35747	1	(1214.4, 948.9)	(1124.9, 923.6)	(1169.6, 936.2)	0.74
35754	1	(1024.3, 1213.8)	(1313.6, 660.7)	(1168.9, 937.2)	0.33

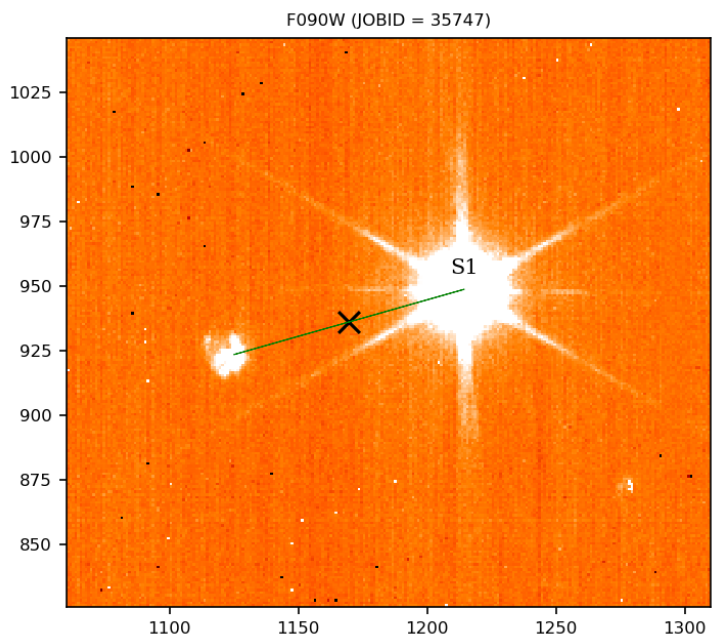

Figure A2-1. The saturated OSIM source for JOBID = 35747 (F090W) is labelled as S1. It is connected to its ghost by the green line. The black X marks the location of the GAP.

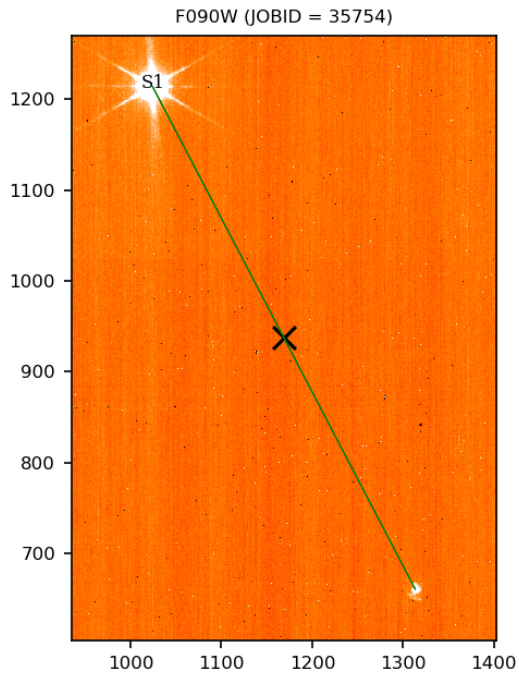

Figure A2-2. Same as Fig. A2-1 but for JOBID = 35754 (F090W).

A2.2 F115W

The properties of the ghosts are summarized in Table A2-3. In this filter, the PSF was pointed at the same location in the field as in the F090W observations. The ghosts are similar to those of F090W but with some differences in their location and morphology. In exposure 35797 (Fig. A2-3), the ghost is doughnut-shaped, reminiscent of an out-of-focus PSF, but asymmetric, and has a diameter of about 20 pixels. As for F090W, the feature at (1276, 873) is also detected. But it is very faint and appears to have a simple, diffuse morphology.

In exposure 35801 (Fig. A2-4), although the bright PSF was moved again by about 325 pixels, a weak, elliptical ghost with a diameter of about 13 pixels is detected, displaced from its location in F090W (Fig. A2-2).

Table A2-3. Sources and Ghosts for F115W (CV3)

JOBID	Number	Source (X, Y)	Ghost (X, Y)	GAP (X, Y)	Ratio (%)
35797	1	(1213.6, 949.0)	(1096.2, 903.5)	(1154.9, 926.2)	0.26
35801	1	(1024.3, 1214.5)	(1286.0, 645.4)	(1155.2, 930.0)	0.018

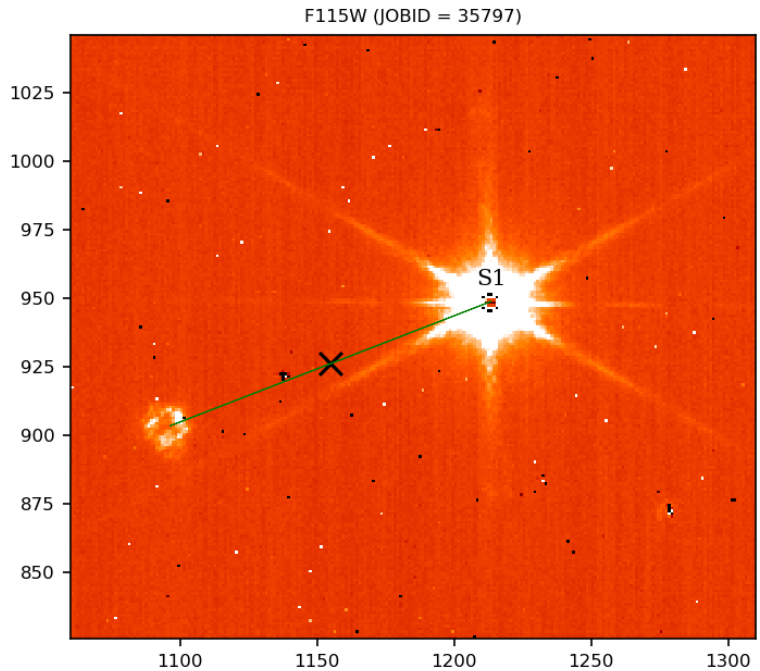

Figure A2-3. Same as Fig. A2-1 but for JOBID = 35797 (F115W).

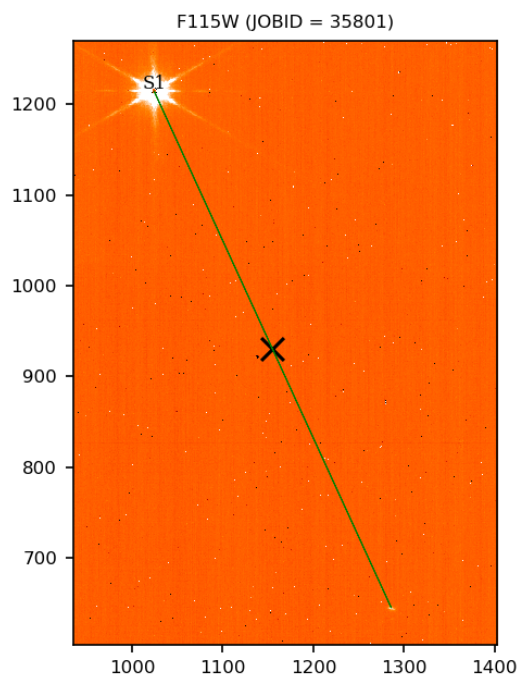

Figure A2-4. Same as Fig. A2-1 but for JOBID = 35801 (F115W).

A2.3 F140M

The properties of the ghosts are summarized in Table A2-4. Again, the source was pointed at the same coordinates as for the previous filters. In JOBID = 35882, the ghost is clearly detected, even in the low-flux image (JOBID = 35881). But unlike F090W and F115W, it appears more comet-like with a prominent knot and a tail (Fig. A2-5), rather than the more circular

morphology depicted above. In JOBID = 35884, the ghost is very faint and nucleated (Fig. A2-6). It is also detected in its counterpart low-flux exposure (JOBID = 35883) as a low-surface brightness blob.

Surprisingly, both ghosts are detected with unsaturated high-flux PSFs so we can accurately and directly measure their relative counts without fitting the low-flux PSF wings or scaling the counts with the TPT scaling factor. Small boxes were simply defined around the source and its ghost and their counts were summed. From the direct measurements, we find ratios of 0.58% and 0.15% for JOBIDs = 35882 and 35884, respectively (Table A2-4). For comparison, we find that the ratios calculated with the TPT scaling factor are 0.62% and 0.18%. This good agreement lends some credence to our use of the TPT scaling factor to calculate the relative strength of the ghosts in the other filters.

Table A2-4. Sources and Ghosts for F140M (CV3)

JOBID	Number	Source (*X*, *Y*)	Ghost (*X*, *Y*)	GAP (*X*, *Y*)	Ratio[1] (%)
35882	1	(1213.8, 948.7)	(1126.2, 918.9)	(1170.0, 933.8)	0.58
35884	1	(1024.1, 1214.4)	(1316.0, 657.4)	(1170.0, 935.9)	0.15

1. The ghost/source ratio is calculated directly from the unsaturated, high-flux PSF, i.e., no scaling factor.

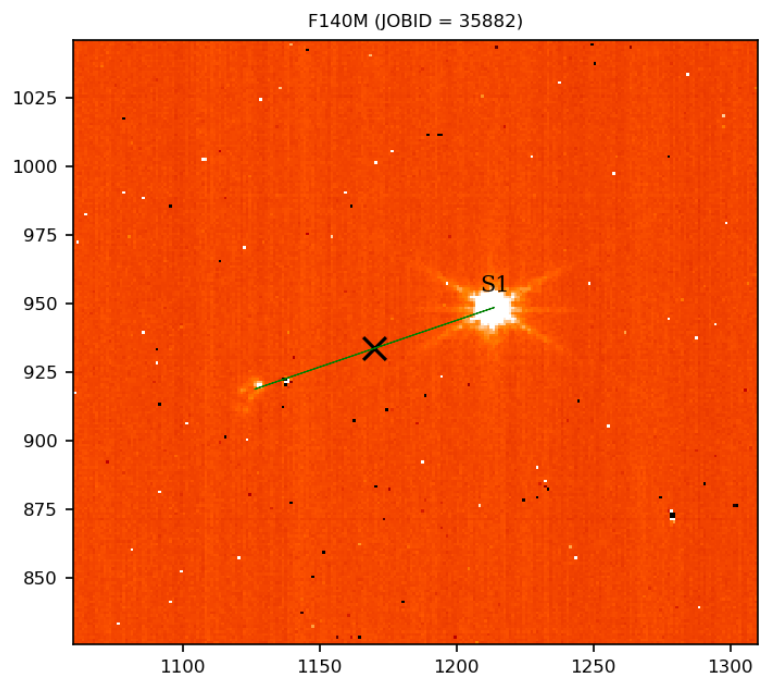

Figure A2-5. Same as Fig. A2-1 but for JOBID = 35882 (F140M).

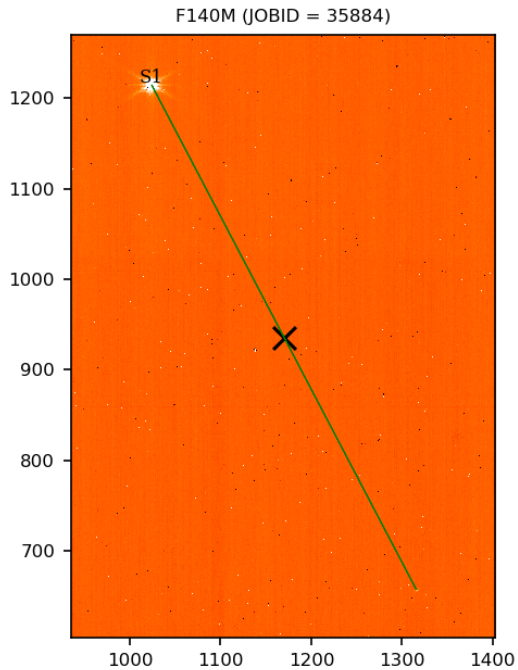

Figure A2-6. Same as Fig. A2-1 but for JOBID = 35884 (F140M).

A2.4 F150W

The properties of the ghosts are summarized in Table A2-5. The OSIM sources were again pointed at the same coordinates in the FOV. In JOBID = 35941, the ghost consists of three large knots and its diameter is about 20 pixels horizontally (Fig. A2-7). In JOBID = 35945, the ghost consists of two compact knots separated by about 10 pixels (Fig. A2-8).

Table A2-5. Sources and Ghosts for F150W (CV3)

JOBID	Number	Source (*X*, *Y*)	Ghost (*X*, *Y*)	GAP (*X*, *Y*)	Ratio (%)
35941	1	(1213.6, 948.7)	(1108.8, 922.8)	(1161.2, 935.8)	0.63
35945	1	(1024.6, 1214.1)	(1297.3, 658.6)	(1160.9, 936.4)	0.34

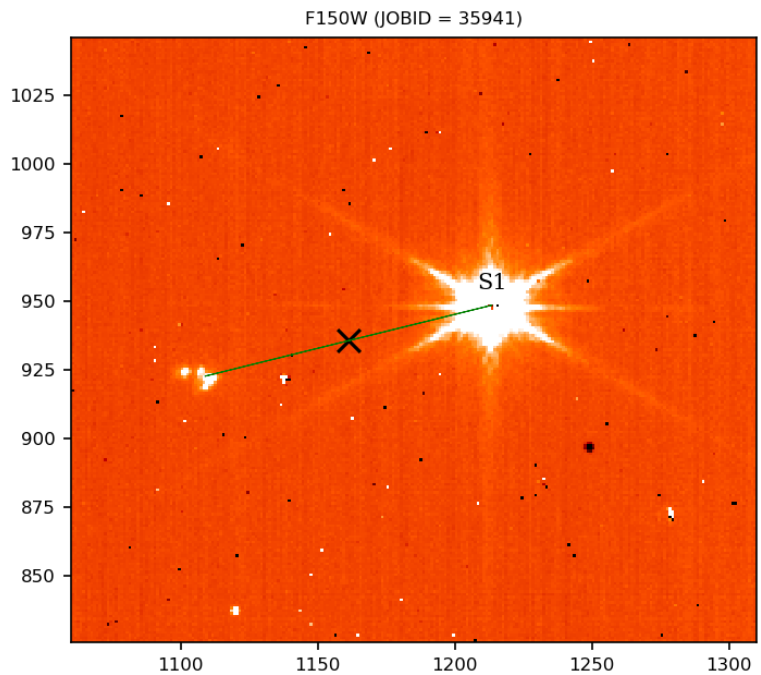

Figure A2-7. Same as Fig. A2-1 but for JOBID = 35941 (F150W).

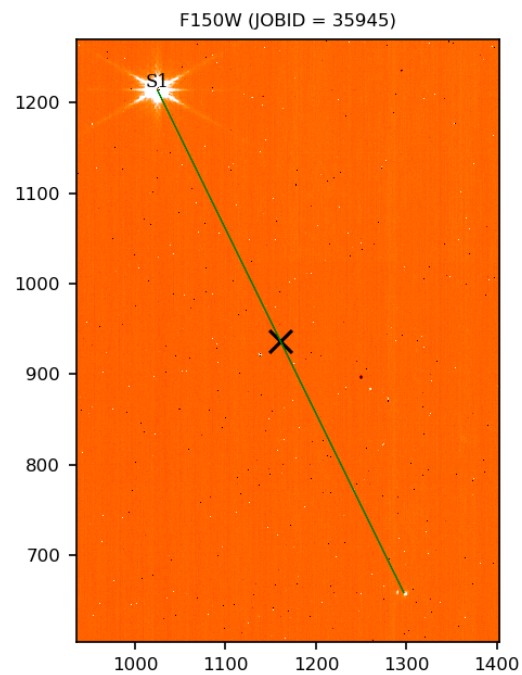

Figure A2-8. Same as Fig. A2-1 but for JOBID = 35945 (F150W).

A2.5 F200W

The properties of the ghosts are summarized in Table A2-6. The exposures for F200W are the last of the OTP 7.6 series and the pointing of the OSIM source is the same as for the other filters. The ghosts are generally more extended and knottier than in the other filters. In JOBID = 35993, the ghost consists of four large knots and spans about 40 pixels (Fig. A2-9). As for some of the other filters, the diffuse and elongated feature at the fixed coordinates of (1276, 873) is also

detected. Similarly, in JOBID = 35996, the ghost spans about 30 pixels and is broken into three large, well-separated clumps, with diameters of about 5 – 15 pixels each (Fig. A2-10). We note that the unsaturated, low-flux PSFs of JOBIDs = 35991 and 35995 produce very faint ghosts.

Table A2-6. Sources and Ghosts for F200W (CV3)

JOBID	Number	Source (*X*, *Y*)	Ghost (*X*, *Y*)	GAP (*X*, *Y*)	Ratio (%)
35993	1	(1211.4, 950.6)	(1101.0, 933.7)	(1156.2, 942.2)	1.4
35996	1	(1022.5, 1215.6)	(1290.6, 671.0)	(1156.5, 943.2)	0.97

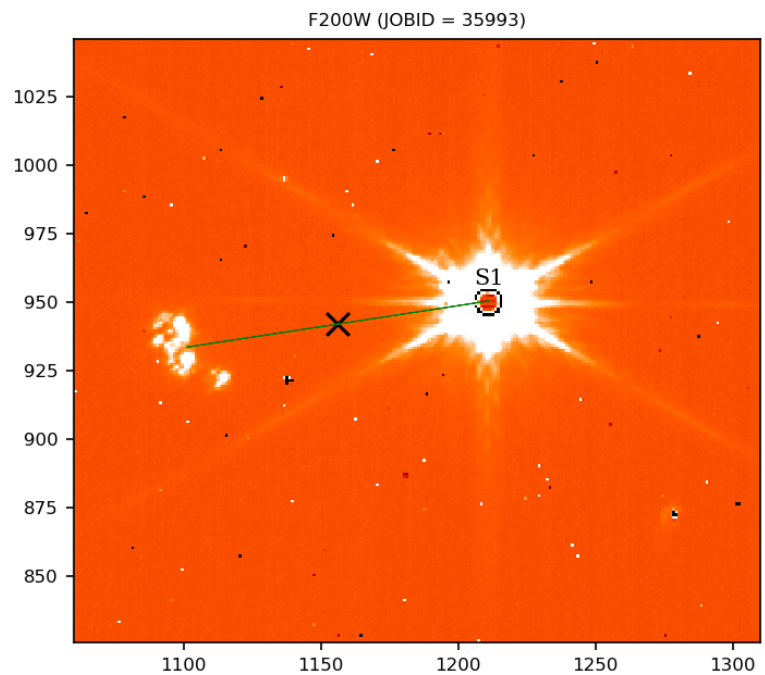

Figure A2-9. Same as Fig. A2-1 but for JOBID = 35993 (F200W).

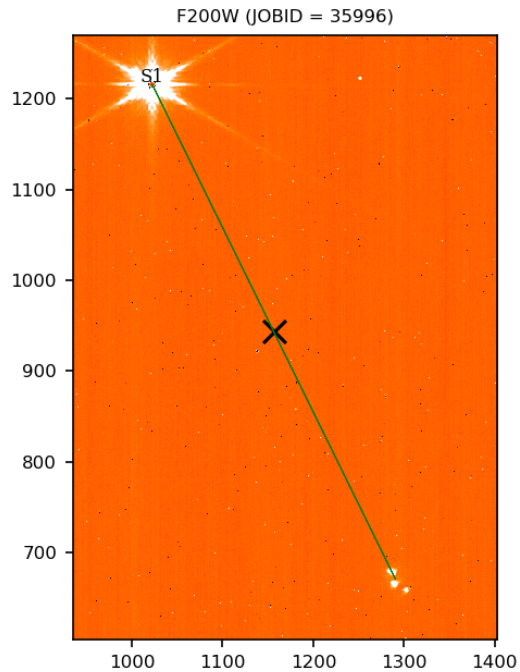

Figure A2-10. Same as Fig. A2-1 but for JOBID = 35996 (F200W).

Appendix 3
CV2 Campaign Data

A catalogue of the exposures with ghosts in the imaging filters is compiled in Table A3-1. As for the CV3 test campaign, the exposures were primarily collected as part of the characterization of the WFSS grisms (GR150C/R) in OTP 7.10.* at the cold plateau (37.2K) (Martel et al. 2014). The PSFs were delivered by OSIM and pointed near the field center and in the four quadrants of the detector. But only the central pointing produced a ghost and these are the exposures that we list in Table A3-1. We note that in this campaign, NIRISS was equipped with a non-flight detector badly contaminated by a large population of RC pixels. These were mostly removed by the subtraction of contemporaneous background exposures.

Table A3-1. Catalogue of Low- and High-Flux OSIM Sources (CV2)

PW	FW	OTP	OSIM Source[1]	JOBID[2]
F090W	CLEAR	7.10.1.1	TUNG (p)	17706, 17708
F115W	CLEAR	7.10.1.4	TUNG (c)	17766, 17768
F150W	CLEAR	7.10.1.5	TUNG (c)	17845, 17847
F200W	CLEAR	7.10.1.5	TUNG (c)	17904, 17902

1. The OSIM source is the continuum tungsten source (TUNG). The illumination is either continuous (c) or pulsed (p).
2. The JOBIDs of the exposure with the low-flux PSF (left entry) and of its high-flux counterpart (right entry) are tabulated.

In Tables A3-2 to A3-5, we tabulate the centroid of the sources and their corresponding ghosts, the coordinates of the GAP, as well as the ratio of their counts. As for the CV3 data, the ratio is calculated by scaling the total counts in the low-flux PSF to its high-flux counterpart using the TPT scaling factor.

A3.1 F090W

The morphology of the ghost is very similar to that observed in CV3 (Section A2.1). The ghost has a rough spiral shape and has a diameter of about 20 pixels (Fig. A2-1). But it appears more dominant than in CV3 (ratio of 1.1%). Along X, the coordinate of the GAP is very close to that in CV3 but about 8 pixels higher along Y.

Table A3-2. Sources and Ghosts for F090W (CV2)

JOBID	Number	Source (X, Y)	Ghost (X, Y)	GAP (X, Y)	Ratio (%)
17708	1	(951.2, 1213.5)	(1387.3, 675.7)	(1169.3, 944.6)	1.1

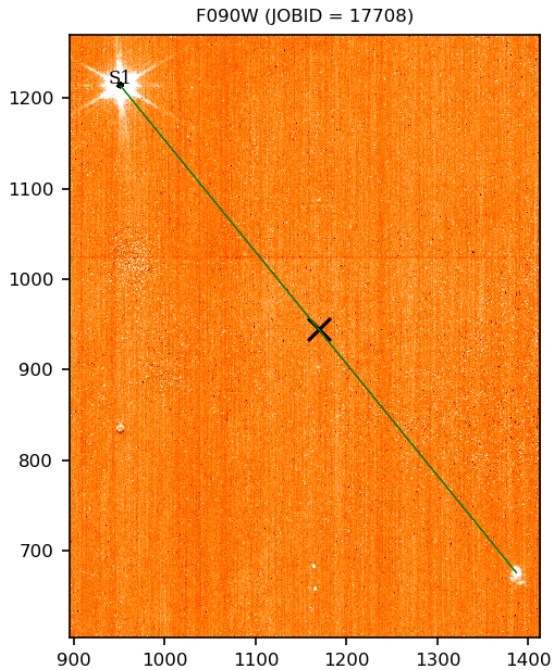

Figure A3-1. The saturated OSIM source for JOBID = 17708 (F090W) is labelled as S1. It is connected to its ghost by the green line. The black X marks the location of the GAP.

A3.2 F115W

In this exposure, the ghost is very weak and elliptical, as in Fig. A2-4, and barely visible above the background level. It has a diameter of about 13 pixels (Fig. A3-2). As for F090W, the Y-coordinate of the GAP is higher than in CV3 by a few pixels.

Table A3-3. Sources and Ghosts for F115W (CV2)

JOBID	Number	Source (X, Y)	Ghost (X, Y)	GAP (X, Y)	Ratio (%)
17768	1	(951.6, 1213.8)	(1359.6, 658.0)	(1155.6, 935.9)	0.066

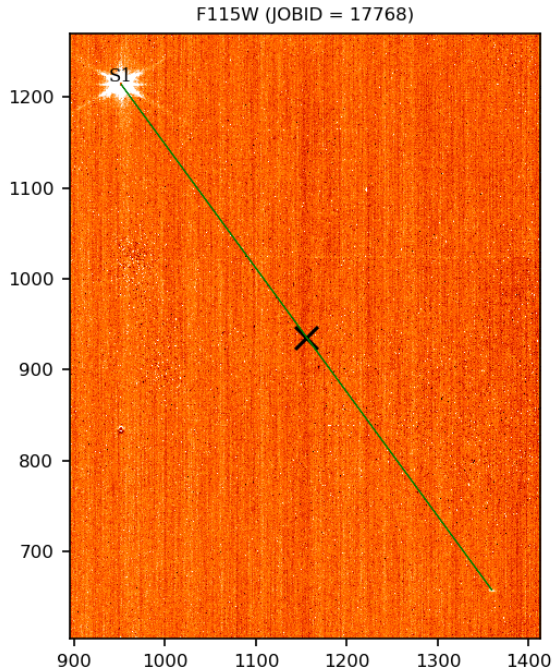

Figure A3-2. Same as Fig. A3-1 but for JOBID = 17768 (F115W).

A3.3 F150W

The ghost is very weak and simply looks like a small clump with no distinctive morphological features (Fig. A3-3). Its diameter is about 6 pixels.

Table A3-4. Sources and Ghosts for F150W (CV2)

JOBID	Number	Source (*X*, *Y*)	Ghost (*X*, *Y*)	GAP (*X*, *Y*)	Ratio (%)
17847	1	(951.3, 1213.8)	(1374.6, 670.4)	(1163.0, 942.1)	0.46

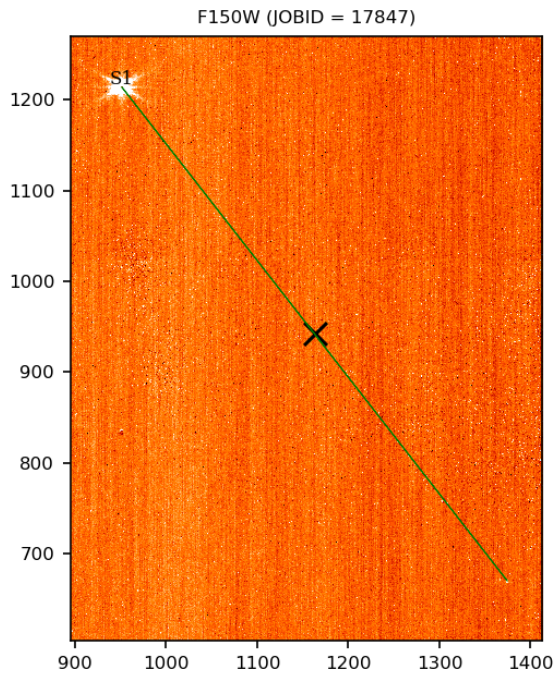

Figure A3-3. Same as Fig. A3-1 but for JOBID = 17847 (F150W).

A3.4 F200W

The ghost is nearly identical to the one seen in CV3 (JOBID = 35996; Fig. A2-10). It spans about 30 pixels and consists of three clumps separated by about 13 pixels (Fig. A3-4). Again, the Y-coordinate of the GAP is higher than in CV3 by about 7 pixels.

Table A3-5. Sources and Ghosts for F200W (CV2)

JOBID	Number	Source (X, Y)	Ghost (X, Y)	GAP (X, Y)	Ratio (%)
17902	1	(950.0, 1214.7)	(1364.4, 685.0)	(1157.2, 949.8)	0.73

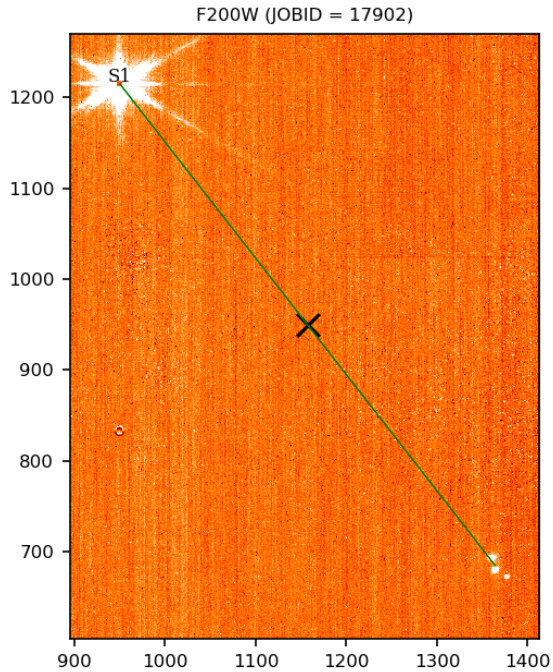

Figure A3-4. Same as Fig. A3-1 but for JOBID = 17902 (F200W).

Appendix 4
CV1RR Campaign Data

In this Appendix, we summarize the ghosts observed with the imaging filters in the CV1RR campaign. The relevant exposures are summarized in Table A4-1. The coordinates of the source, its ghost, and the GAP are also tabulated. Because the government shutdown greatly reduced the scope of the NIRISS activities, mostly high-flux, saturated PSFs were imaged with the simple goal of detecting ghosts. The centroids are therefore estimated visually and the ratio of the counts between the ghost and the PSF cannot be reliably measured.

Table A4-1. Location of the Sources and Ghosts in CV1RR

OTP	JOBID	PW	FW	Source (*X*, *Y*)	Ghost 1 (*X*, *Y*)	GAP (*X*, *Y*)	Ghost 2 (*X*, *Y*)
7.6 Rev A	7031	F090W	CLEAR	(1056, 1257)	(1284, 632)	(1170.0, 944.5)	(1221, 1253)
0.2.1.1	5309	F115W	CLEAR	(1012, 1026)	(848, 644)	(930.0, 835.0)	–
0.2.1.1	5314	F115W	CLEAR	(1013, 1026)	(851, 643)	(932.0, 834.5)	–
7.6 Rev C	7044	F115W	CLEAR	(1056, 1257)	(1258, 614)	(1157.0, 935.5)	–
7.10	7130	F115W	CLEAR	(605, 1368)	(1700, 505)	(1152.5, 936.5)	(770, 1366)
7.10	7131	F115W	CLEAR	(1687, 380)	–	–	(1854, 374)
7.10	7136	F115W	CLEAR	(846, 761)	(1467, 1102)	(1156.5, 931.5)	(1012, 758)
7.13	7150	F115W	CLEAR	(1063, 1345)	(1250, 529)	(1156.5, 937.0)	–
0.2.1.1	5318	F140M	CLEAR	(1012, 1025)	(1330, 855)	(1171.0, 940.0)	–
0.2.1.1	5323	F140M	CLEAR	(1012, 1025)	(1330, 855)	(1171.0, 940.0)	–
7.7	7070	F140M	CLEAR	(1055, 1258)	(1285, 625)	(1170.0, 941.5)	–
7.10	7137	F140M	CLEAR	(1228, 440)	(1115, 1438)	(1171.5, 939.0)	–
7.10	7121	F158M	CLEAR	(1041, 433)	(1255, 195)	(1148.0, 314.0)	–
7.10	7122	CLEARP	F277W	(740, 1266)	(1651, 1943)	(1195.5, 1604.5)	–
7.5	6987	CLEARP	F380M	(1096, 845)	(1234, 1054)	(1165.0, 949.5)	–
7.5	6996	CLEARP	F430M	(1096, 845)	(1234, 1054)	(1165.0, 949.5)	–
7.5	6983	CLEARP	F480M	(1091, 859)	(1239, 1046)	(1165.0, 952.5)	–
7.5	6985	CLEARP	F480M	(1096, 845)	(1234, 1052)	(1165.0, 948.5)	–
7.13	7141	CLEARP	F480M	(1083, 1215)	(1306, 1999)	(1194.5, 1607.0)	–
7.13	7142	CLEARP	F480M	(1020, 1187)	(1368, 2027)	(1194.0, 1607.0)	–

In the following figures, some of the saturated CV1RR PSFs and their associated ghosts are shown for the filters that are not well presented in the other cryo test campaigns. As before, we label the source as S1 and its primary ghost as 1 and we use this ghost to locate the GAP. A small circular blob (~6 pixels in diameter), possibly a ghost (ghost 2 in Table A4-1), is seen in F090W (Fig. A4-1) and F115W. This blob is about 165 pixels (10.7″) immediately to the right of the PSF in both filters and is brighter in the hemisphere pointing towards the PSF.

In Fig. A4-4, the OSIM source was pointed at the same location on the detector, near the field center, for F380M, F430M, and F480M. All three produce essentially identical ghosts. But in Fig. A4-5, the source was imaged at two other locations in F480M and the ghosts now appear near the top edge and with very different morphologies. There may then be two GAPs for the filters of the FW, one near the field center and the other in the upper-right quadrant. The GAP of F277W is also consistent with the latter.Curiously, in two exposures (JOBIDs = 5309 and 5314 in OTP 0.2.1.1), faint blobs are seen at locations that are inconsistent with the GAP measured in F115W, e.g., JOBIDs = 7044, 7130, 7136, 7150. In these two exposures, the PSF is not saturated. Possibly, the features could be due to the OSIM configuration in this First Light activity, a fiber leak, or persistence from a bright source in a previous exposure. We list these exposures in Table A4-1 for future reference in the unlikely event that they are observed in orbit.

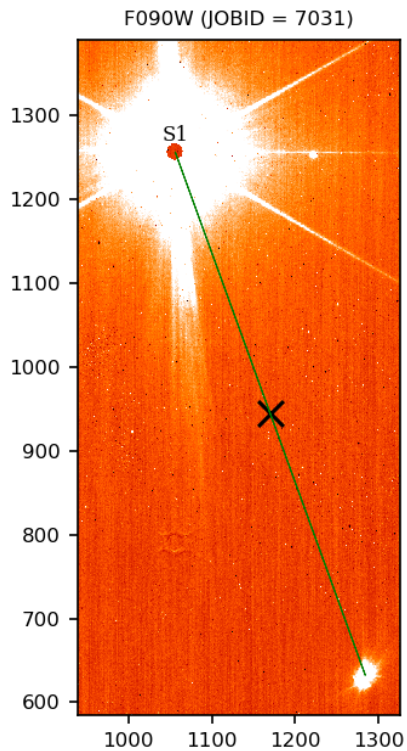

Figure A4-1. The saturated OSIM source for JOBID = 7031 (F090W) is labelled as S1. It is connected to its primary ghost by the green line. The black X marks the location of the GAP. The core of the PSF also manifests itself as crosstalk (the "embossed" circle about 475 pixels below the PSF).

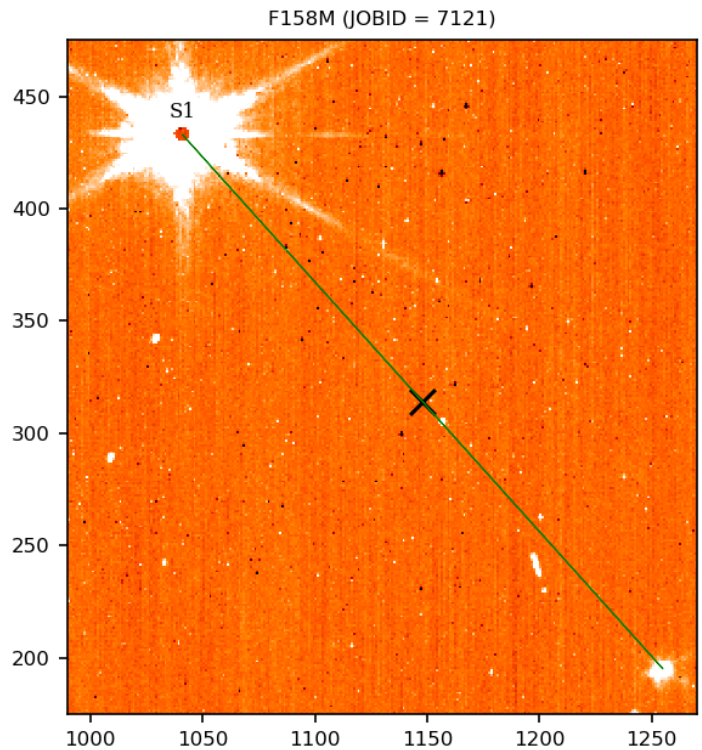

Figure A4-2. Same as Fig. A4-1 but for JOBID = 7121 (F158M).

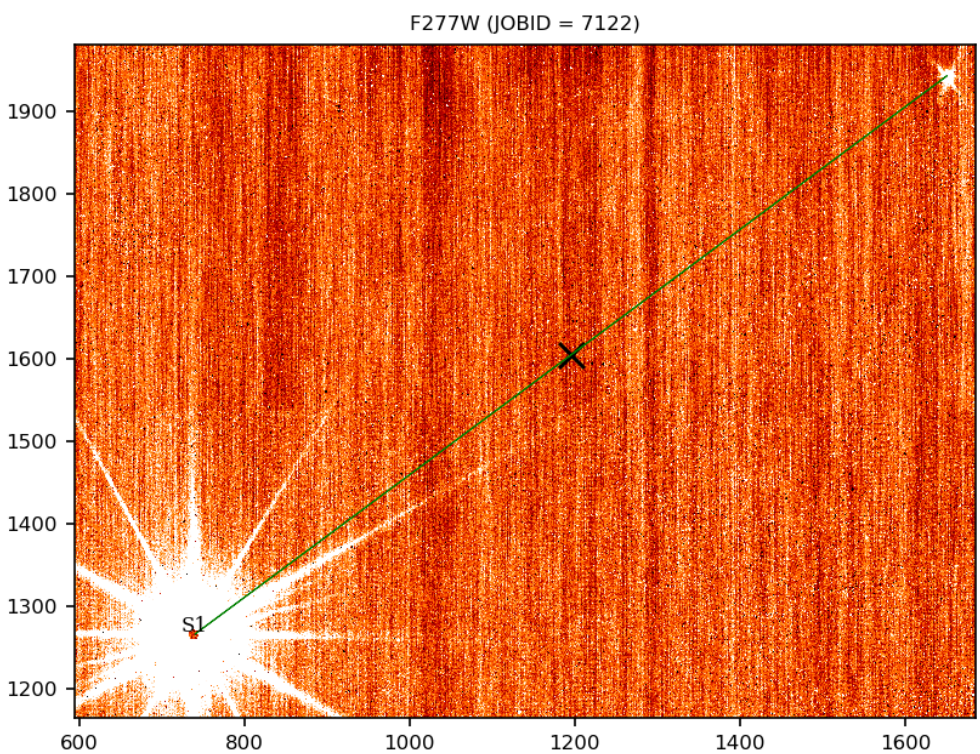

Figure A4-3. Same as Fig. A4-1 but for JOBID = 7122 (F277W).

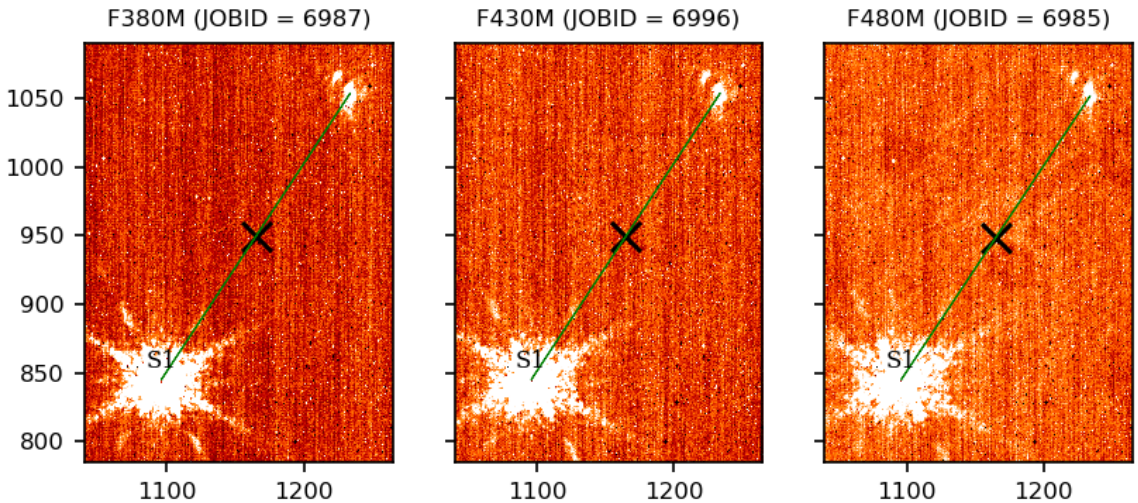

Figure A4-4. Same as Fig. A4-1 but for F380M (left: JOBID = 6987), F430M (middle: JOBID = 6996), and F480M (right: JOBID = 6985). The three exposures were collected as part of the OTP 7.5 activity when the OSIM TUNG2 source was pointed at (1096, 845). The three ghosts have nearly identical locations and morphologies. A hint of the superferrule of the source delivery module of OSIM is visible in the F480M image.

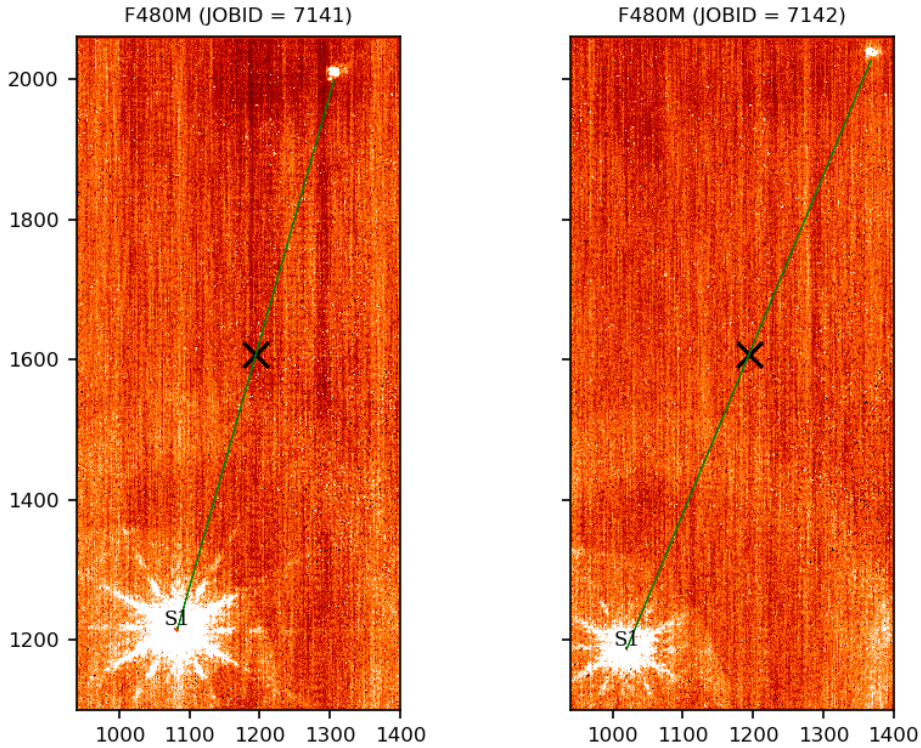

Figure A4-5. Same as Fig. A4-1 but for F480M (left: JOBID = 7141 and right: 7142). The two exposures were collected as part of the OTP 7.13 activity. The PSFs are slightly displaced and the signature of the superferrule is seen as arcs.